



Study on a Damage Model and Uniaxial Compression Simulation Method of Frozen–Thawed Rock

Qiang Feng¹ · Jichao Jin¹ · Shuang Zhang¹ · Weiwei Liu¹ · Xuxu Yang¹ · Weiteng Li¹

Received: 9 April 2021 / Accepted: 8 September 2021 / Published online: 6 October 2021
© The Author(s), under exclusive licence to Springer-Verlag GmbH Austria, part of Springer Nature 2021

Abstract

To evaluate the deterioration degree of rock freeze–thaw damage in cold area engineering, it is necessary to establish an accurate freeze–thaw rock damage model and its uniaxial compression numerical simulation method. Therefore, indoor freeze–thaw cycle tests of saturated yellow sandstone were carried out. The porosity and P-wave velocity were measured, and uniaxial compression tests were conducted after different numbers of freeze–thaw cycles. The findings indicate that with an increasing number of freeze–thaw cycles, the elastic modulus, peak strength and wave velocity of the yellow sandstones gradually decrease, while the peak strain and the average porosity increase. The energy evolution law with different numbers of freeze–thaw cycles was analyzed, a freeze–thaw damage model was established according to the relative change in the dissipated energy ratio before and after freezing–thawing, and the accuracy of this damage model and five common damage models was evaluated by the uniaxial compressive strength and peak strain. The functional relationship between mesoscopic parameters and the number of freeze–thaw cycles was formulated to establish a numerical simulation method for saturated sandstones under uniaxial compression after freeze–thaw cycling. The reliability of the numerical method was verified by comparing the stress–strain curve, peak stress, peak strain and energy law with the experimental results.

Keywords Freeze–thaw cycle test · Energy analysis · Dissipated energy ratio damage model · Accuracy evaluation · Numerical simulation method

1 Introduction

Western China’s rapid development has led to an increasing number of resource mining operations and the construction of large-scale infrastructure projects in cold regions. However, freeze–thaw cycles have posed a great threat to the stability of rock mass engineering in cold regions (Liu et al. 2019). Furthermore, numerous freeze–thaw cycles have the potential to cause a series of geological engineering problems, such as weathering and destabilization of rock slopes (Krautblatter et al. 2013; Pudasaini and Krautblatte 2014). Hence, the accurate representation of freeze–thaw damage on rocks and the establishment of a reliable uniaxial compression numerical simulation method under freeze–thaw

conditions have become key concerns in engineering projects in cold regions.

In recent years, scholars worldwide have made significant strides in studying the damage models of quasi-brittle materials such as rocks, and these advancements can be summarized by five damage models. (1) Static elastic modulus damage model: Many studies have shown that there is a certain relationship between the static elastic modulus and material damage (Kachanov 1958; Tan et al. 2011). Lemaitre (1984) introduced the strain equivalence assumption, which provides a theoretical framework for developing damage models with the static elastic modulus as an evaluation index. Wang et al. (2020) used the static elastic modulus to present the damage evolution of rock under cyclic loading. (2) Porosity damage model: The porosity test for rocks generally includes oven-drying and nuclear magnetic resonance tests (Ke et al. 2017; Li et al. 2018). Jia et al. (2015) developed a fatigue damage model using sandstone porosity to thoroughly explore the coupling methods of high-cycle and low-cycle fatigue damage. Matsuoka (1990) represented the rock damage rate with the porosity. (3) P-wave

✉ Weiwei Liu
skd994491@sdust.edu.cn

¹ Shandong Key Laboratory of Civil Engineering Disaster Prevention and Mitigation, School of Civil Engineering and Architecture, Shandong University of Science and Technology, Qingdao 266590, China

velocity damage model: Many scholars have measured the P-wave velocity of rocks and concrete at different numbers of freeze–thaw cycles to quantify the damage (Remy et al. 1994; Takarli et al. 2008; Pan et al. 2019). Kawamoto et al. (1988) established a quantitative relationship between wave velocity and rock damage based on the isotropy assumption. Inserra et al. (2013) represented the damage degree of the material with the wave velocity and temperature. (4) Dynamic-elastic modulus damage model: According to the *Standard for Test Methods of Long-Term Performance and Durability of Ordinary Concrete* (GB/T 50082-2009) in China, the antifreeze grade of concrete can be determined to be at its maximum number of freeze–thaw cycles when the relative dynamic elastic modulus drops to no less than 60%. Hassanzadegan et al. (2014) established the relationship between the dynamic elastic modulus and wave velocity and density. This study provides a basis for the development of damage models with a dynamic elastic modulus. Petersen et al. (2007) used the relative dynamic elastic modulus to quantitatively represent the freeze–thaw damage of concrete. (5) Energy damage model: The dissipated energy is usually used to evaluate the energy dissipation and damage accumulation of rocks at each deformation stage (Khazaei et al. 2015; Chen et al. 2016; Wang et al. 2017). Gao et al. (2020) established a freeze–thaw damage model with the energy dissipation ratio. Deng et al. (2019) studied the variation rule of elastic modulus, total strain energy, releasable elastic strain energy and dissipated energy of rocks with the number of freeze–thaw cycles through experiments and used the total energy to characterize freeze–thaw damage of rocks. In general, there are fewer systematic analyses on the accuracy of the damage models in current achievements.

In terms of numerical simulation methods, the physicochemical and mechanical changes of materials during freezing have been the focus of research. Zuber and Marchand (2004) established the relationship between pore water pressure and the icing volume during the freezing process with the finite element method. Duan et al. (2013) developed a coupled thermo-hydro-mechanical (THM) model with COMSOL Multiphysics for the concrete freezing process and investigated the change in temperature distribution, unfrozen water volume and strain with freezing time. The deepening of these studies motivated scholars to begin material damage simulations of the freeze–thaw cycle process. Fan et al. (2013) investigated the effect of freeze–thaw cycles on stress with ANSYS to predict the cracking of concrete. Wang et al. (2016) analyzed the effects of freeze–thaw cycles on foundation settlement and slope stability using FLAC3D and represented the freeze–thaw damage with changes in the elastic modulus. Qiu et al. (2020) analyzed freeze–thaw damage by equating the ratio of plastic strain to inelastic strain in concrete under compression as

a freeze–thaw damage factor with ABAQUS. Lin et al. (2020) performed several freeze–thaw simulations by equating the expansion coefficient to the freeze expansion force with PFC and used the frost heaving force to represent the freeze–thaw damage of rocks. Notably, there are relatively few research results of numerical methods for simulating the freeze–thaw damage of rocks.

In this paper, the physical and mechanical properties of saturated yellow sandstones after a number of freeze–thaw cycles were tested. A freeze–thaw damage model was established using the relative change in the dissipated energy ratio according to the energy analysis results. The accuracy of the damage model in this paper and other common models was evaluated by the peak strength and peak strain of the rock as evaluation parameters. The quantitative relationship between three mesoscopic parameters (parallel-bond normal strength, parallel-bond tangential strength, and stiffness ratio) and the number of freeze–thaw cycles was formulated through numerical tests, and then a numerical simulation method of uniaxial compression of saturated sandstones after freeze–thaw cycling was established. The reliability of the method was verified via comparison of the calculation results with the test results. This study can aid in analyzing the mechanism involved in the freeze–thaw damage of rocks and serve as a reference for engineering designs in cold regions.

2 Test Methods and Results

2.1 Processing and Screening of Rock Samples

In this study, yellow sandstones were taken as test samples. The sandstones were processed into cylindrical standard samples with a diameter of 50 ± 0.3 mm and a height of 100 ± 0.3 mm in accordance with the *Rock Test Procedure for Water Resources and Hydropower Engineering* (SL264-2001). The end surface of each sample was perpendicular to its axis, with the deviation controlled within 0.25° , and the unevenness of the end surface was within 0.05 mm. The porosity, permeability, density and P-wave velocity of the samples were measured. Last, a group of samples that featured good uniformity, as shown in Fig. 1, was selected for freeze–thaw cycle testing. Table 1 lists the average parameters of the selected samples.

2.2 Composition Test of Rock Sample

XRD and SEM tests were carried out on the selected rock samples. Figure 2 shows the rock X-ray diffraction pattern. The test results show that the proportions of α -quartz, stishovite, α -tridymite, β -tridymite and kaolinite are 83.8, 1.3, 2.3,

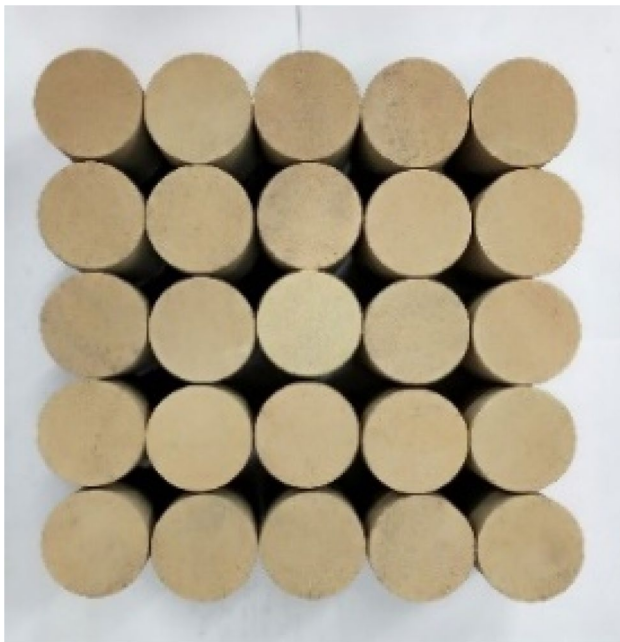


Fig. 1 Selected samples

Table 1 Average parameters of rock samples

Parameter	Average density (g/cm ³)	Porosity/%	Permeability/mD	Average P-wave speed/(m/s)
Mean	2.34	9.80	2.40	2970

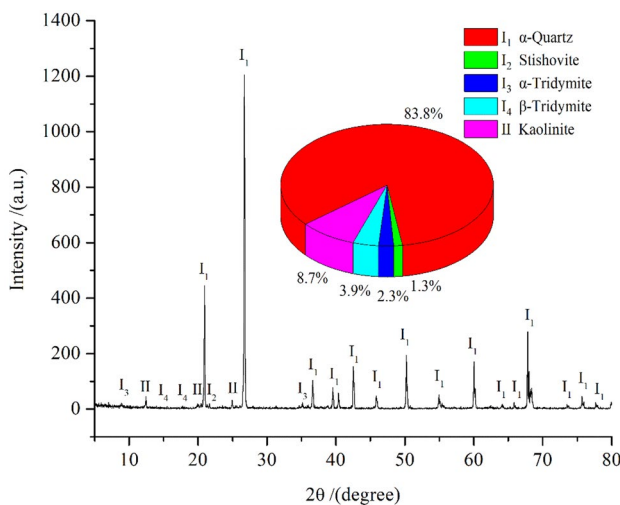


Fig. 2 X-ray diffraction pattern

3.9 and 8.7%, respectively. The 2000 \times and 30,000 \times meso scanning results of the rock samples are shown in Fig. 3. The rock has a layered structure and is relatively dense overall.

2.3 Test Instruments

The test instruments mainly included (1) a high- and low-temperature test chamber (as shown in Fig. 4a) from Shanghai Linpin Instrument Stock Co., Ltd., with a temperature range from $-40\text{ }^{\circ}\text{C}$ to $150\text{ }^{\circ}\text{C}$ and a temperature rise rate of $1\text{--}3\text{ }^{\circ}\text{C}/\text{min}$; (2) a TAW-1000 micro electrohydraulic servo-controlled rock triaxial pressure tester (as shown in Fig. 4b) with an axial displacement range of 30 mm and an axial pressure of 2000 kN; (3) a 5058PR high-voltage ultrasonic pulse generator/receiver (as shown in Fig. 4c); and (4) a gas porosity tester (as shown in Fig. 4d), with an error of $\pm 0.5\%$ and a porosity measurement range of 0.01–40%.

2.4 Parameters of the Freeze–Thaw Cycle Tests

1. The test simulated the temperatures in Xinjiang, China. According to data from the China Meteorological Administration, July is the hottest month, with the average highest temperature reaching $30\text{ }^{\circ}\text{C}$. The temperatures in January and December are the lowest, with an average monthly minimum temperature of $-20\text{ }^{\circ}\text{C}$ and a historical minimum temperature of $-30\text{ }^{\circ}\text{C}$ in Xinjiang. Therefore, the temperature for this freeze–thaw cycle test was determined to be -30 to $30\text{ }^{\circ}\text{C}$.
2. By testing the temperature at the center of each sample, it was found that the freezing and thawing of the samples required 4 h. The heating and cooling process of the instrument took 30 min. Therefore, it was concluded that the time for each freeze–thaw cycle was 9 h. The freeze–thaw time–temperature curve is shown in Fig. 5.

2.5 Test Steps

The specific test steps are shown as follows:

1. The samples were saturated at -0.1 MPa for 6 h, then soaked at atmospheric pressure for 18 h, and finally wiped dry after being taken out.
2. To avoid the subsequent mechanical test results being affected by the process of drying and then saturation during the porosity test, the specimens were divided into two groups (C and K). Group C was used for the P-wave velocity test and uniaxial compression test, and group K was used for the pore test; the details are provided in Table 2.
3. Group K was placed into the high- and low-temperature test chamber for 0, 20, 40, 60 and 100 freeze–thaw cycles. Then, the samples were placed into a drying oven with the drying temperature set at $108\text{ }^{\circ}\text{C}$, and the porosity of the samples was measure.
4. Group C was placed into the high- and low-temperature test chamber for 0, 20, 40, 60 and 100 freeze–thaw

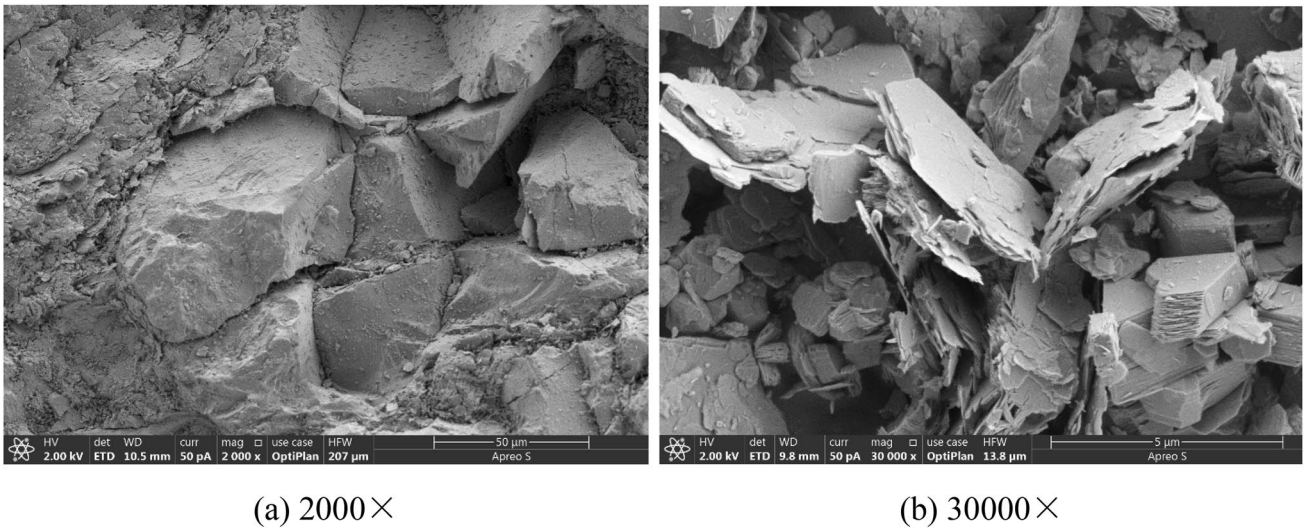
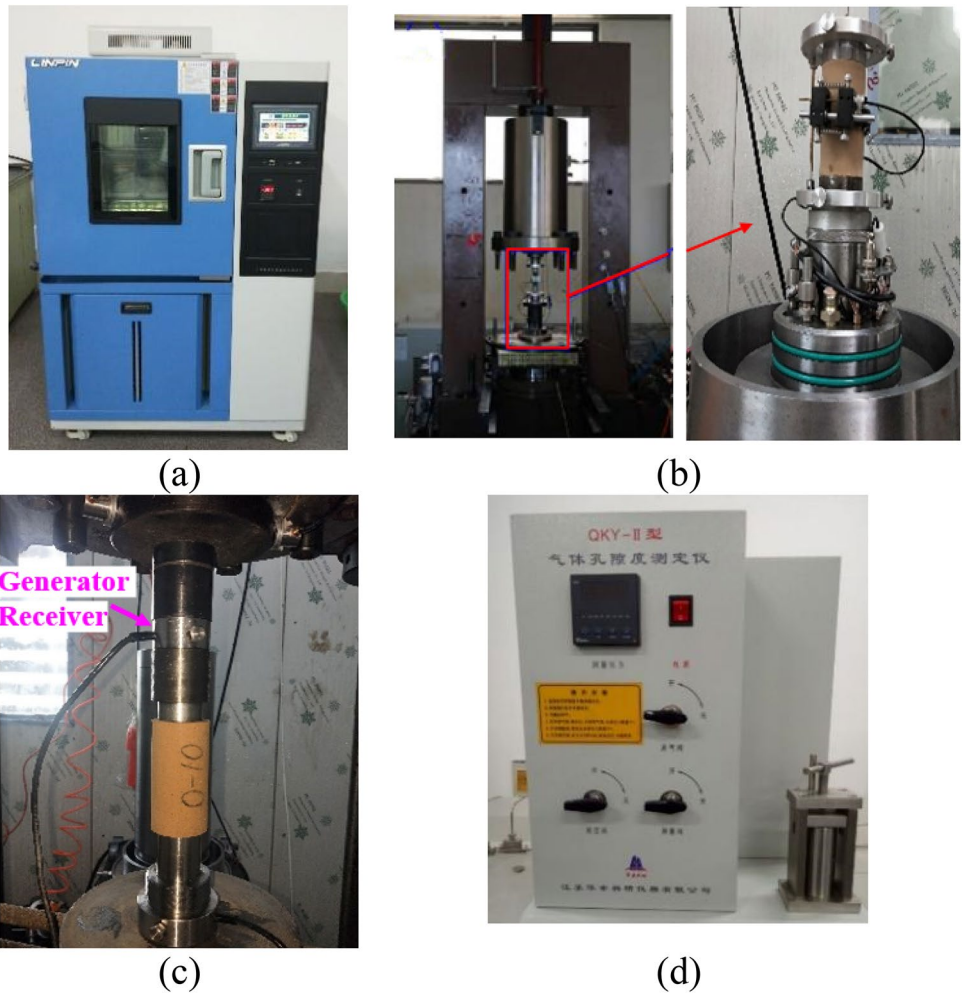


Fig. 3 SEM results

Fig. 4 Main test instruments: **a** high- and low-temperature alternating damp heat test chamber; **b** rock triaxial pressure tester; **c** ultrasonic pulse generator/receiver; **d** gas porosity tester



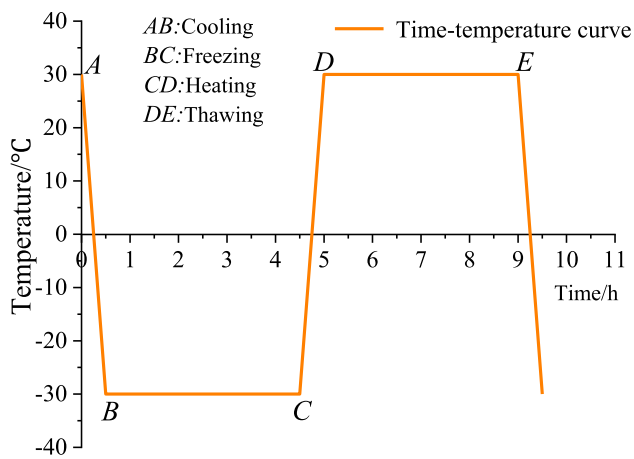


Fig. 5 Freeze–thaw temperature–time curve

cycles. When the freeze–thaw cycle number reached 0, 20, 40 and 60 cycles, C1–C3 were removed to test the P-wave velocity. Due to subsequent supplementary tests, when the freeze–thaw cycle reached 100 cycles, the rock samples tested for wave velocity were C13–C15.

- Uniaxial compression tests were conducted on group C in displacement loading mode (with a loading rate of 0.1 mm/min) until the samples were damaged.

2.6 Test Results

2.6.1 Failure Mode

The failure modes of rocks after different numbers of freeze–thaw cycles under uniaxial compression are shown in Fig. 6.

According to the failure modes of rocks shown in Fig. 6, the following can be seen: (1) The rock samples

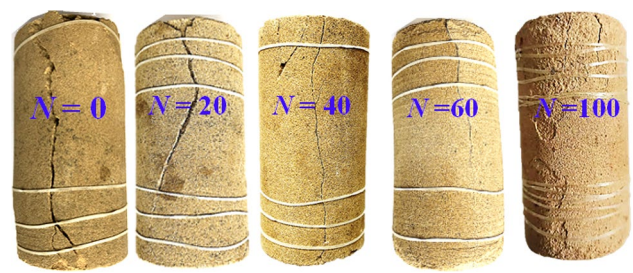


Fig. 6 Failure modes of frozen–thawed rocks under uniaxial compression

show splitting failure modes under different numbers of freeze–thaw cycles, indicating that the number of freeze–thaw cycles has no obvious influence on rock failure modes; and (2) With the increase in the number of freeze–thaw cycles, the crack opening of the rock samples decreases, indicating that freeze–thaw cycling reduces the elastic strain energy stored in the rock sample at the time of failure and the degree of failure, which is consistent with conclusions in the literature (Deng et al. 2019).

2.6.2 Stress–Strain Curve

The stress–strain curves of yellow sandstones after different numbers of freeze–thaw cycles are shown in Fig. 7. The test results show that, after 0, 20, 40, 60 and 100 freeze–thaw cycles, the uniaxial compressive strength of saturated sandstones gradually decreases. The peak strain gradually increases and the elastic moduli gradually decrease (Table 3 for specific data). The above data indicate obvious freeze–thaw damage to sandstones and highlight that reasonable quantization of freeze–thaw damage holds great significance for evaluating the stability of engineering projects in cold regions.

Table 2 Test grouping of different rock samples

Number	Number of F–T cycles <i>N</i>	Drying treatment	Physical test	Mechanical test
K1~K3	0	Drying at 108 °C	Porosity test	–
K4~K6	20			
K7~K9	40			
K10~K12	60			
K13~K14	100			
C13~C15	100	–	P-wave velocity test	Uniaxial compression test
C1~C3	60			
C4~C6	40			
C7~C9	20			
C10~C12	0			

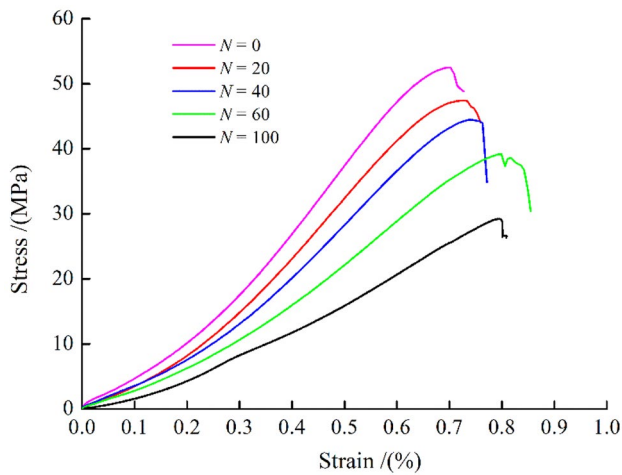


Fig. 7 Stress–strain curve of sandstones under different numbers of freeze–thaw cycles

Table 3 Effect of the number of freeze–thaw cycles on uniaxial compressive strength, peak strain and elastic modulus of sandstones

Number	0	20	40	60	100
Peak intensity/MPa	52.49	47.40	44.45	39.21	29.21
Peak strain/%	0.702%	0.728%	0.738%	0.798%	0.796
Elastic modulus/GPa	10.51	8.98	8.29	6.57	4.85

Table 4 Effect of the number of freeze–thaw cycles on the porosity of sandstones

Number of freeze–thaw cycles	Sample no	Porosity/%	Average porosity/%	Porosity increment/%
0	K1	10.00	9.80	0
	K2	9.90		
	K3	9.50		
20	K4	10.50	10.20	0.4
	K5	10.19		
	K6	9.9		
40	K7	10.78	10.51	0.71
	K8	10.45		
	K9	10.30		
60	K10	11.20	11.00	1.2
	K11	10.70		
	K12	11.10		
100	K13	12.02	12.08	2.28
	K14	12.13		

2.6.3 Porosity

The porosities of sandstones after different numbers of freeze–thaw cycles are shown in Table 4. The test results

indicate that, after 0, 20, 40, 60 and 100 freeze–thaw cycles, the average porosity of saturated sandstones gradually increases to 9.8, 10.20, 10.51, 11.00 and 12.08%, respectively. For the number of freeze–thaw cycles specified in the test, the porosity increments of saturated sandstone were 0.4, 0.31, 0.49 and 1.08%.

2.6.4 P-Wave Velocity

The P-wave velocities of sandstones after a certain number of freeze–thaw cycles are shown in Table 5. The test results demonstrate that, after 0, 20, 40, 60 and 100 freeze–thaw cycles, the average P-wave velocity of saturated sandstones gradually decreases, and the attenuation rate of the wave velocity gradually increases.

3 Establishment of Freeze–Thaw Damage Models

The law of energy evolution is often applied to analyze the deformation and failure of rocks in mechanics tests. Compared with the traditional stress and strain analysis methods, this method analyzes the failure process of rock from the perspective of energy accumulation and dissipation, which is more aligned with the nature of rock failure. Therefore, the progressive law of rock damage can be better revealed by establishing a damage factor from energy.

3.1 Energy Calculation

Throughout the test, the deformation of the rock mass can be divided into two parts: reversible deformation and irreversible deformation. In reversible deformation, the energy is mainly transformed into elastic strain energy in the samples. When irreversible deformation occurs, some portion of the energy is mainly dissipated in the forms of plastic deformation, damage, friction and thermal radiation, which is called dissipated energy (Bai 2015). According to the first law of thermodynamics, if the heat exchange with the external environment in the process is ignored, then the total energy input by the testing machine in the process of rock deformation is converted only into the elastic strain energy and dissipated energy inside the rock (Xie et al. 2005):

$$U = U^e + U^d \quad (1)$$

where U is the total energy input from the outside (in kJ/m^3); U^e is the elastic strain energy (in kJ/m^3); and U^d is the dissipated energy (in kJ/m^3). The distribution of U , U^e and U^d in the stress–strain curve is shown in Fig. 8.

Table 5 Effect of the number of freeze–thaw cycles on the wave velocity

Number of freeze–thaw cycles	Sample No	P-wave velocity/(m/s)	Average P-wave velocity/(m/s)	Attenuation rate of wave velocity%
0	C1	2744	2724	0
	C2	2727		
	C3	2701		
20	C1	2661	2647	2.83
	C2	2654		
	C3	2630		
40	C1	2594	2598	4.62
	C2	2580		
	C3	2570		
60	C1	2475	2440	10.43
	C2	2425		
	C3	2420		
100	C13	2060	2065	24.22
	C14	2068		
	C15	2068		

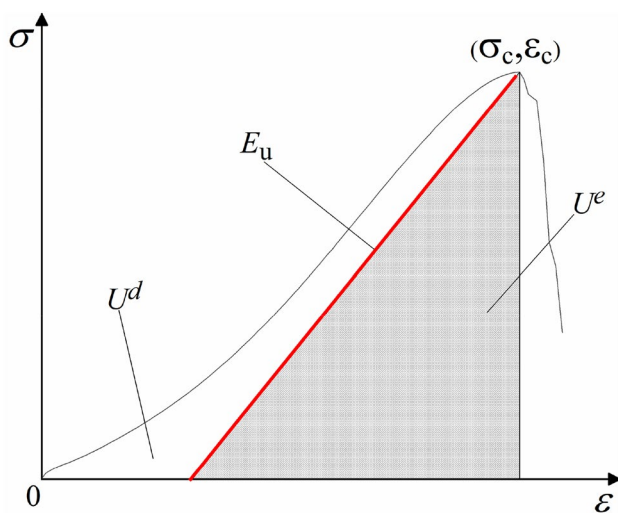


Fig. 8 Relationship between releasable elastic strain energy and dissipated energy in the stress–strain curve

The total energy absorbed by the rock samples during the test is:

$$U = \int_0^{\epsilon_1} \sigma \, d\epsilon \tag{2}$$

According to the theory of elasticity, the elastic strain energy stored in the rock samples can be expressed as:

$$U^e = \frac{\sigma_1^2}{2E_u} \tag{3}$$

In Eq. (2) and Eq. (3), σ_1 and ϵ_1 are the axial stress and the axial strain, respectively. E_u is the unloading modulus, which is generally approximated by the elastic modulus E .

3.2 Energy Evolution Law for Sandstones after Freeze–Thaw cycles

3.2.1 Process of Energy Evolution

Based on the results shown in Table 3, the uniaxial compressive strength, peak strain and elastic modulus of sandstones after different numbers of freeze–thaw cycles are substituted into Eqs. (1)–(3) to calculate the total energy, elastic strain energy and dissipated energy during uniaxial compression, respectively. Figure 9 shows the evolution of stress and various energy indices with strain under different numbers of freeze–thaw cycles.

Combining the characteristics of rock stress–strain curves, the energy evolution process of sandstone after freeze–thaw cycling can be divided into four stages:

1. Section OA is the initial compression stage of the stress–strain curve, during which a part of the energy imposed on the rock sample by the testing machine is converted into elastic strain energy, and the remaining energy is dissipated due to the closure of primary cracks in the rock sample. In this stage, the elastic strain energy is basically equal to the dissipated energy as the strain increases.
2. Section AB is the elastic stage of the stress–strain curve, during which, with increasing strain, the elastic strain energy grows much larger than the dissipated energy.

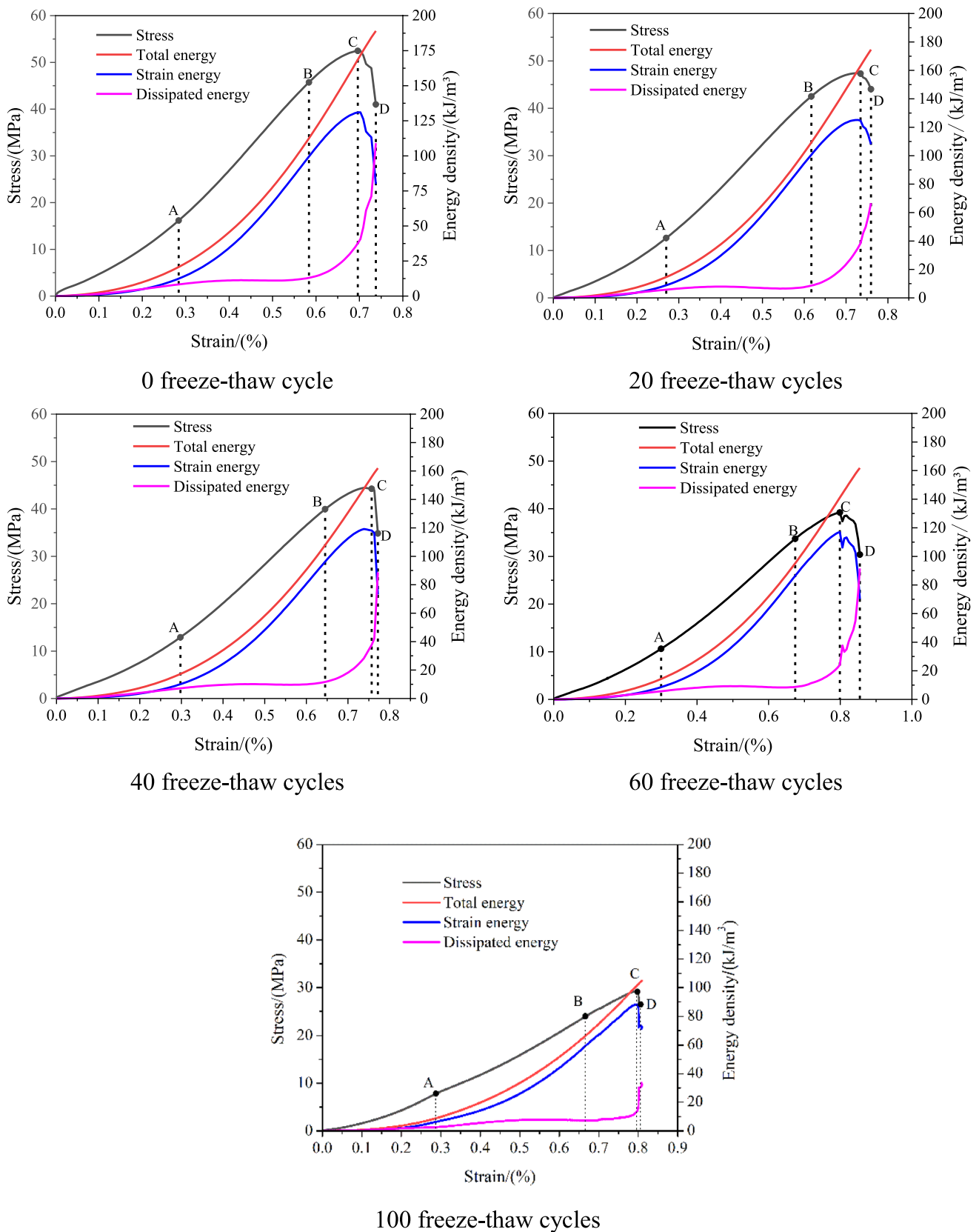


Fig. 9 Evolution of stress and energy in sandstones after different numbers of freeze-thaw cycles

The total energy and the elastic strain energy gradually increase at similar growth rates, and the dissipated energy curve is approximately horizontal. These changes suggest that the total energy is mostly converted into elastic strain energy and that the dissipated energy has basically remained constant.

3. Section BC is the hardening stage of the stress–strain curve. In this stage, as the load continues to increase, the sandstone exhibits obvious plastic deformation. With increasing axial strain, the elastic strain energy increases at a slowing rate, and the dissipated energy increases at a substantial rate. The elastic strain energy reaches its maximum value in the vicinity of the peak strength, which indicates that the accumulated energy of the rock sample has reached its limit.
4. Section CD is the strain softening stage of the stress–strain curve. As the strain increases, the elastic strain energy curve decreases sharply, while the dissipated energy conversely increases. The reason is that the cracks in the sandstone extend through after the peak point, and the elastic strain energy stored in the rock sample is rapidly released in the forms of kinetic energy, friction energy, and heat energy of the rock mass, which ultimately leads to loss of the load-bearing capacity (Xie et al. 2005).

3.2.2 Relationship Between the Pre-peak Energy and the Number of Freeze–Thaw Cycles

The results calculated from Eqs. (1)–(3) are shown in Table 6.

The change curves of pre-peak total energy, elastic strain energy and dissipated energy with the number of freeze–thaw cycles are shown in Fig. 10.

Mutlutürk et al. (2004) developed a first-order model for the freeze–thaw damage prediction of rocks, as shown in Eq. (4). Altindag et al. (2004) used such a prediction model for fitting analysis of the uniaxial compressive strength, uniaxial tensile strength, point load strength, and P-wave velocity of ignimbrite after 0 to 55 freeze–thaw cycles. This approach resulted in goodness of fit values of 0.97, 0.97,

Table 6 Elastic modulus and energy values of rock samples under different number of freeze–thaw cycles

Number of freeze–thaw cycles	E_p /GPa	U /(kJ/m ³)	U^e /(kJ/m ³)	U^d /(kJ/m ³)
0	10.51	171.77	131.09	40.68
20	8.98	160.26	125.10	35.16
40	8.29	147.54	119.22	28.32
60	6.57	141.14	117.01	24.13
100	4.85	101.35	88.03	13.32

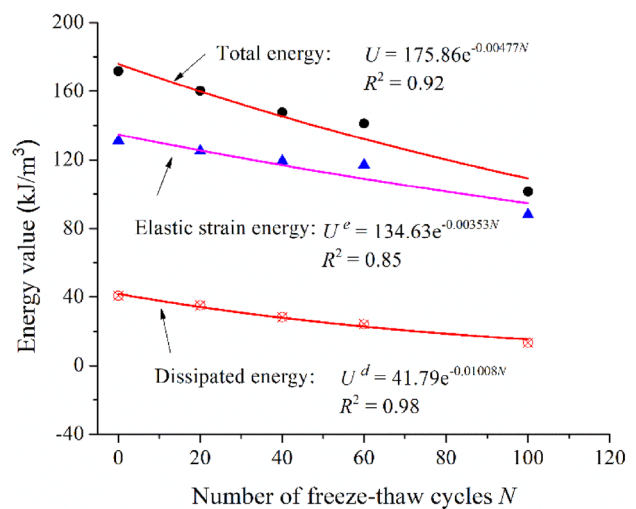


Fig. 10 Change in peak energy with the number of freeze–thaw cycles

0.92 and 0.96, which indicates the reliability of such a first-order model for the prediction of freeze–thaw damage.

$$I_N = I_0 e^{-\lambda N} \tag{4}$$

where N is the number of freeze–thaw cycles; $e^{-\lambda N}$ is the attenuation factor, indicating the proportion of remaining integrity at the N th freeze–thaw cycle; I_0 and I_N are the integrity indices of the rocks before and after the freeze–thaw cycle, respectively; and λ is the attenuation constant. The pre-peak total energy, elastic strain energy and dissipated energy were fitted based on the above model, and the results were as follows:

$$U = 175.86e^{-0.00477N}, \quad (R^2 = 0.92) \tag{5}$$

$$U^e = 134.63e^{-0.00353N}, \quad (R^2 = 0.85) \tag{6}$$

$$U^d = 41.79e^{-0.01008N}, \quad (R^2 = 0.98) \tag{7}$$

where N is the number of freeze–thaw cycles.

The results show that the pre-peak total energy gradually decreases as the number of freeze–thaw cycles increases. This finding indicates that freeze–thaw cycling intensifies the deterioration of the rock, resulting in a decrease in the energy that needs to be absorbed from outside to destroy the rock sample. The proportion of elastic strain energy increases gradually, while the proportion of dissipated energy decreases gradually, indicating that freeze–thaw cycling increases the proportion of energy used for deformation and reduces the severity of failure. This assessment is consistent with the analysis results based on rock failure photographs.

3.3 Damage Model Based on the Dissipated Energy Ratio

To facilitate the analysis of the energy mechanism of freeze–thaw damage to rocks, the dissipated energy ratio after different numbers of freeze–thaw cycles is defined as λ_N : the ratio of peak dissipated energy to the total energy after different freeze–thaw cycles (i.e., Eq. 8).

$$\lambda_N = \frac{U_N^d}{U_N} \quad (8)$$

where U_N and U_N^d are the total energy and dissipated energy after N freeze–thaw cycles, respectively.

Substituting Eqs. (5) and (7) into Eq. (8) yields:

$$\lambda_N = 0.24e^{-0.00531N} \quad (9)$$

Its change law is shown in Fig. 11.

From the perspective of thermodynamics, energy dissipation is unidirectional and irreversible and is mainly applied for the plastic deformation and crack extension of rocks. Hence, freeze–thaw damage factors can be established based on the relative change in the dissipated energy ratio of rocks before and after freeze–thaw cycles. However, the change law of the dissipated energy ratio is uncertain due to the decrease in peak strength, the increase in peak strain and the decrease in elastic modulus after freezing–thawing. A freeze–thaw damage model is established as follows based on the above analysis:

$$D = \frac{|\lambda_N - \lambda_0|}{\lambda_0} \quad (10)$$

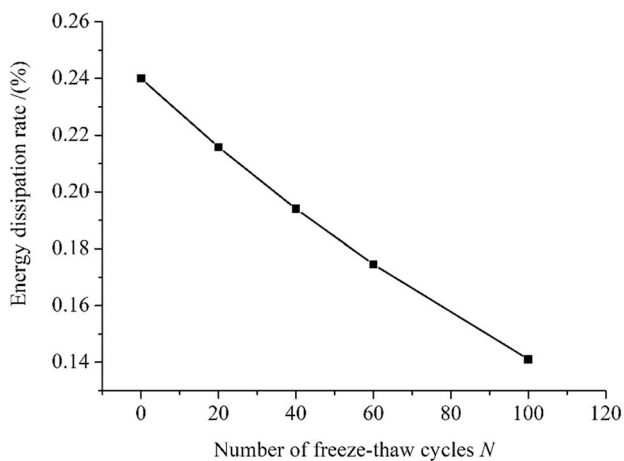


Fig. 11 Relationship curve of the energy dissipation rate and number of freeze–thaw cycles

Substituting Eq. (9) into Eq. (10) yields the evolution equation of freeze–thaw damage in sandstones:

$$D = 1 - e^{-0.00531N} \quad (11)$$

According to the *Code for Design of Railway Tunnels* (TB10003-2016), the designed service life of the retaining wall and lining should be 100 years, while that of the side elevation slope should be 60 years. The *Standard for Design of Concrete Structure Durability* (GB/T50476-2019) specifies that, the design reference period of cement concrete for a freeze–thaw environment should be 30, 50 or 100 years. According to this regulation, different projects in cold regions have different service lives, and the longest time is 100 years. Therefore, the maximum number of freeze–thaw cycles in this test is set to 100. The change in the damage factors established based on the dissipated energy ratio with the number of freeze–thaw cycles is shown in Fig. 12. When $N = 30, 50, 60$ and 100, the freeze–thaw damage factors of sandstone are 0.15, 0.24, 0.28 and 0.42, respectively.

4 Model Accuracy Evaluation

In engineering practice, the accurate estimation of rock deterioration based on established damage factors significantly impacts the stability of engineering projects in cold regions.

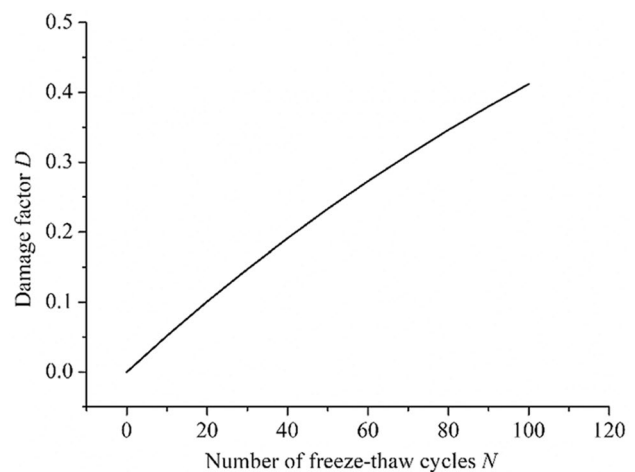


Fig. 12 Damage evolution curve based on the dissipation energy rate

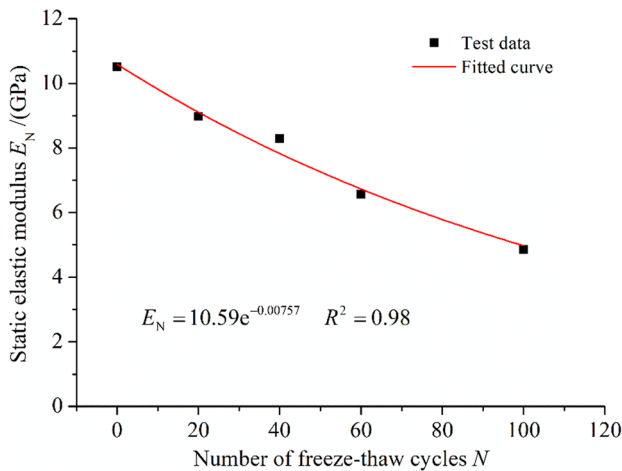


Fig. 13 Change in static elastic modulus with the number of freeze–thaw cycles

4.1 Freeze–Thaw Damage Factors Calculated Based on Other Models

According to the test results, the freeze–thaw damage factors are generally calculated based on the static elastic modulus damage model, porosity damage model, P-wave velocity damage model, dynamic elastic modulus damage model and total energy.

1. Damage factors established based on the static elastic modulus.

According to the test results in Table 3, the number of freeze–thaw cycles was fitted with the static elastic modulus according to Eq. (4), and the results are shown in Fig. 13. The fitting equation is shown as follows:

$$E_N = 10.59e^{-0.00757N}, \quad (R^2 = 0.98) \quad (12)$$

Based on the strain equivalence assumption (Lemaiter, 1984), the freeze–thaw damage can be expressed with the static elastic modulus as follows:

$$D = 1 - \frac{E_N}{E_0} \quad (13)$$

where D is the damage factor of freeze–thaw cycles, ranging from 0 to 1. When $D=0$, the sample is intact; however, when $D=1$, the sample is completely damaged. E_0 and E_N are the static elastic modulus of sandstones at the 0th freeze–thaw cycle and at the N th freeze–thaw cycle, respectively.

Substituting Eq. (12) into Eq. (13) yields the evolution equation of freeze–thaw damage in sandstones:

$$D = 1 - 1.008e^{-0.00757N} \quad (14)$$

2. Damage factors established based on porosity.

The porosity test results (Table 4) reveal the change in the average porosity of sandstones after different numbers of freeze–thaw cycles as shown in Fig. 14. The relationship between the average porosity and the number of freeze–thaw cycles can be expressed by regression fitting as:

$$p_N = 9.719 + 0.0227N, \quad (R^2 = 0.98) \quad (15)$$

where p_N is the porosity of sandstones at the N th freeze–thaw cycle, %.

From the perspective of damage mechanics and based on the concept of effective reduction in loading zones, Zhang et al. (2020) defined sandstone porosity damage variables in a freeze–thaw environment as:

$$D = \frac{v_N - v_0}{v_N + v_r - v_0} \quad (16)$$

where D is the freeze–thaw damage factor, v_0 is the pore volume of sandstones at the 0th freeze–thaw cycle, v_N is the pore volume of sandstones at the N th freeze–thaw cycle, and v_r is the volume of sandstones.

The rock porosity can be expressed as:

$$p = 1 - \frac{v_s}{v_r} \quad (17)$$

where v_s is the volume of the rock skeleton.

Substituting Eq. (17) into Eq. (16) yields:

$$D = 1 - \frac{1}{1 + p_N - p_0} \quad (18)$$

where p_0 is the porosity of sandstones at the 0th freeze–thaw cycle.

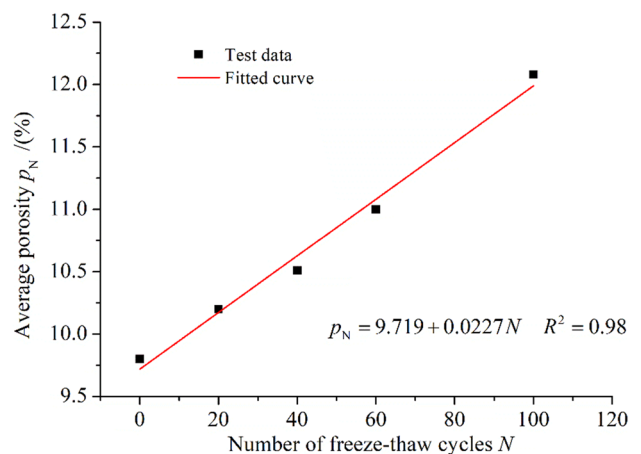


Fig. 14 Change in average porosity with the number of freeze–thaw cycles

Substituting Eq. (15) into Eq. (18) yields the evolution equation of freeze–thaw damage in sandstones:

$$D = 1 - \frac{1}{0.99919 + 0.000227N} \tag{19}$$

3. Damage factors established based on P-wave velocity.

The results of the P-wave velocity tests shown in Table 5 reveal the change curve of the average P-wave velocity of sandstones with different numbers of freeze–thaw cycles, as shown in Fig. 15. The number of freeze–thaw cycles is fitted to the average P-wave velocity according to the model shown in Eq. (4) to obtain:

$$V_{pN} = 2790.42e^{-0.00264N}, \quad (R^2 = 0.89) \tag{20}$$

where V_{pN} is the P-wave velocity of the sandstone at the N th freeze–thaw cycle.

Kawamoto et al. (1988) assumed a rock to be an isotropic body composed of parent materials and microcracks and thus defined the freeze–thaw damage variable of sandstones according to the P-wave velocity as:

$$D = 1 - \frac{V_{pN}^2}{V_{p0}^2} \tag{21}$$

where V_{p0} is the average P-wave velocity of the sandstone at the 0th freeze–thaw cycle.

Substituting Eq. (20) into Eq. (21) yields the evolution equation for freeze–thaw damage in sandstones:

$$D = 1 - 1.02e^{-0.00264N} \tag{22}$$

4. Damage factors established based on the dynamic elastic modulus.

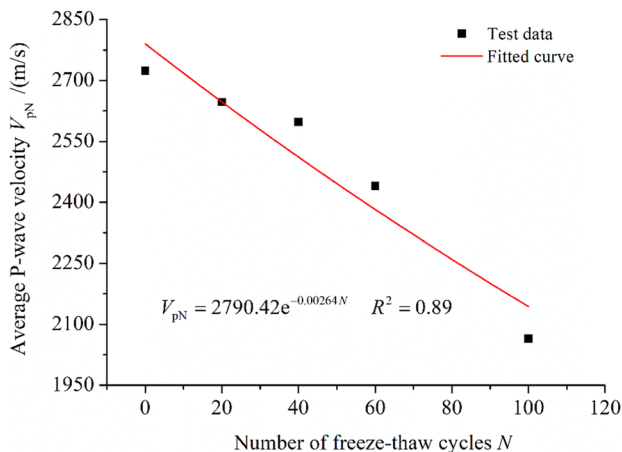


Fig. 15 Change in average P-wave velocity with the number of freeze–thaw cycles

Based on the damage mechanics theory, the damage variable is defined with the dynamic elastic modulus of the rock as:

$$D = 1 - \frac{E_{dN}}{E_{d0}} \tag{23}$$

where D is the freeze–thaw damage factor of the rock and E_{d0} and E_{dN} are the dynamic elastic modulus of sandstone at the 0th freeze–thaw cycle, and at the N th freeze–thaw cycle, respectively.

Based on elasticity theory, the dynamic elastic modulus can be expressed as:

$$E_d = \frac{\rho V_{pN}^2 (1 + \lambda)(1 - 2\lambda)}{1 - \lambda} \tag{24}$$

where ρ is the rock density and λ is the rock Poisson’s ratio.

Without regard to the changes in the rock Poisson’s ratio before and after freeze–thaw cycles, substituting Eq. (24) into Eq. (23) yields:

$$D = 1 - \frac{\rho_N V_{pN}^2}{\rho_0 V_{p0}^2} = 1 - \frac{v_0 V_{pN}^2}{v_N V_{p0}^2} \tag{25}$$

where ρ_0 and ρ_N are the density of the rock at the 0th freeze–thaw cycle, and at the N th freeze–thaw cycle, respectively. v_0 and v_N are the unit mass volumes of the sandstones at the 0th freeze–thaw cycle, and at the N th freeze–thaw cycle, respectively.

Liu et al. (2015) expressed the unit mass volume changes of the sandstone at the 0th freeze–thaw cycle and at the N th freeze–thaw cycle, without considering the change in the matrix:

$$\frac{v_0}{v_N} = \frac{v_s + v_a}{v_s + v_a + \Delta v_a} \tag{26}$$

where v_s and v_a are the volume of the matrix and pore of the unit mass rock before freeze–thaw cycles, respectively; Δv_a is the pore volume change of the rock mass before freeze–thaw cycles.

The porosity of sandstones at the 0th freeze–thaw cycle can be expressed as

$$p_0 = \frac{v_a}{v_s + v_a} \tag{27}$$

The porosity of sandstones at the N th freeze–thaw cycle can be expressed as

$$p_N = \frac{v_a + \Delta v_a}{v_s + v_a + \Delta v_a} \tag{28}$$

Substituting Eqs. (26)–(28) into Eq. (25) derives the freeze–thaw damage variable of sandstones as:

$$D = 1 - \left(\frac{1 - p_N}{1 - p_0} \right) \frac{V_{pN}^2}{V_{p0}^2} \tag{29}$$

Substituting Eq. (15) and Eq. (20) into Eq. (29) derives the freeze–thaw damage evolution equation of sandstones as:

$$D = 1 - (1.0009 - 2.517 \times 10^{-4}N) \times (1.05e^{-0.00528N}) \tag{30}$$

5. Damage factors established based on total energy.

As the number of freeze–thaw cycles increases, sandstone samples require less input energy; therefore, many scholars have established a damage model to calculate the freeze–thaw damage factors based on the total energy change (Wang et al. 2017; Deng et al. 2019).

$$D = 1 - \frac{U_N}{U_0} \tag{31}$$

Substituting Eq. (4) into Eq. (31) derives the freeze–thaw damage evolution equation of sandstones as:

$$D = 1 - 1.024e^{-0.00477N} \tag{32}$$

4.2 Damage Evolution Law

Figure 16 shows the variation in the damage factor established based on the dissipative energy ratio and the other five damage factors with the number of freeze–thaw cycles *N*. The curves show that the damage factor established by porosity is the lowest, while that established by the static

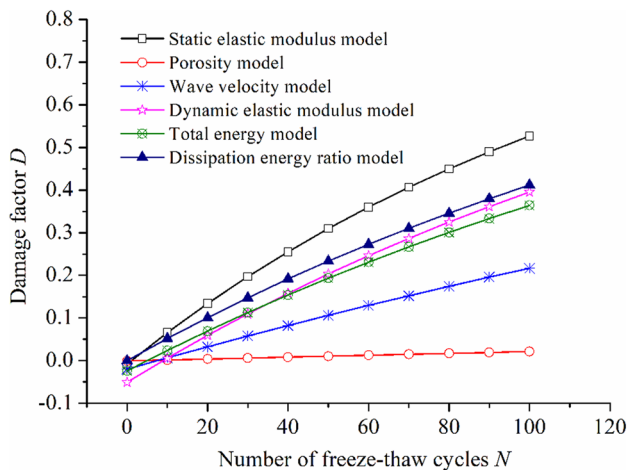


Fig. 16 Evolution curves of damage factors with the number of freeze–thaw cycles in different models

elastic modulus is the highest. The evolution curves of the damage factors established by the dynamic elastic modulus, dissipation energy ratio and total energy are very close. The damage evolution curve represented by P-wave velocity is between those characterized by total energy and porosity. The damage evolution curve represented by the dissipative energy ratio is between those characterized by the static elastic modulus and dynamic elastic modulus.

4.3 Accuracy Evaluation of Damage Factors

According to the experimental data from Deng et al. (2019), the damage evolution curve of the dissipated energy ratio model in this paper and the total energy model adopted in the literature are compared, and the results are shown in Fig. 17. As seen from the shape of the curves, the two damage curves generally increase with the number of freeze–thaw cycles, but the curves are slightly different due to the different fitting equations used by the two methods.

To better evaluate the errors of different damage models and take into account the important influence of uniaxial compression strength and peak strain on the stability of engineering, these two parameters are calculated as the target parameters for accuracy analysis of damage models.

1. Uniaxial compressive strength.

The mechanical strength of sandstone after freeze–thaw cycles is related to the initial strength and the degree of freeze–thaw damage of the rock. Based on the effects of the initial strength of the rock and damage variables, a nonlinear prediction equation for the uniaxial compressive strength of the rock is established based on Eq. (4) as:

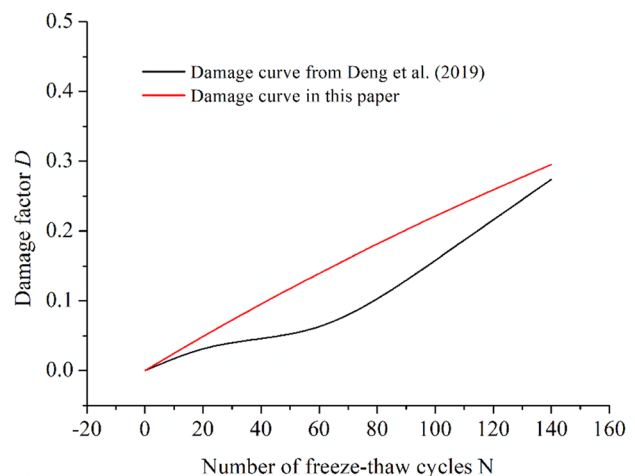


Fig. 17 Comparison of damage curves based on Deng et al. (2019)

$$\sigma_N = \sigma_0(1 - D) \tag{33}$$

where σ_N is the strength of sandstone after N freeze–thaw cycles, and σ_0 is the strength of sandstone that has not been frozen or thawed.

The uniaxial compressive strength of sandstones (see Table 7) after different numbers of freeze–thaw cycles in six models was calculated with the nonlinear prediction equation of uniaxial compressive strength (Eq. 33). The strength of sandstones obtained from the tests was compared with the results calculated by the prediction models, as shown in Fig. 18. Overall, the peak strength calculated based on the damage model of the dissipated energy ratio shows the greatest accuracy when compared with the test results.

2. Peak strain.

Based on the change curve of peak strain versus the number of freeze–thaw cycles, Gao et al. (2020) defined the relative strain variables as:

$$\frac{\epsilon_N - \epsilon_0}{\epsilon_0} = k_N D \tag{34}$$

where ϵ_0 is the peak strain of sandstones at the 0th freeze–thaw cycle; ϵ_N is the peak strain of sandstones at the N th freeze–thaw cycle; and k_N is the freeze–thaw influence coefficient of sandstones at the N th freeze–thaw cycle. Substituting the test data into Eq. (34) yields that k_{20} , k_{40} , k_{60} and k_{100} are 0.3816, 0.3348, 0.5405 and 0.2899, respectively.

Based on Eq. (34), the peak strains calculated with the six models for different numbers of freeze–thaw cycles were compared with the test results, as shown in Table 8 and Fig. 19. As seen in the results, the values of peak

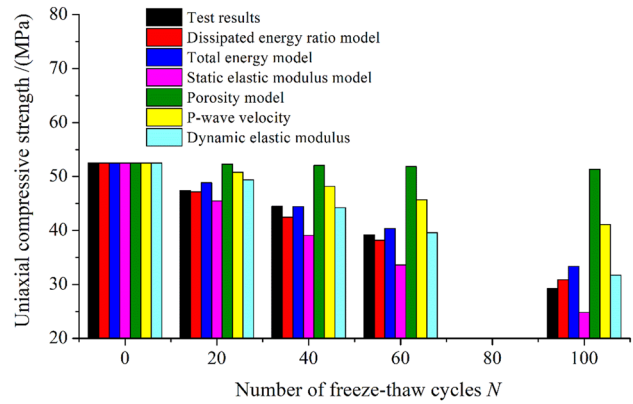


Fig. 18 Comparison diagram of the measured and calculated uniaxial compressive strength

strains predicted based on the energy damage models of dissipated energy ratio have minimum error and are stable when compared with the test results.

5 Numerical Simulation Method for Uniaxial Compression of Rocks Damaged in Freeze–Thaw Cycles

5.1 Preparation of Samples for the Numerical Simulation

Currently, PFC is often used to simulate stress–strain curves, strength and other macro-mechanical properties of sandstone samples. However, the PFC3D simulation method requires substantial time for calculation and has difficulty controlling boundary conditions (Yang et al. 2014; Huang et al. 2017). PFC2D, on the other hand, can provide accurate results and requires a lower calculation cost for models with simple

Table 7 Test and calculated values of uniaxial compressive strength after different numbers of freeze–thaw cycles

Number of freeze–thaw cycles		20	40	60	100
Test value/(MPa)		47.4	44.45	39.21	29.21
Dissipated energy ratio model	Calculated value/(MPa)	47.20	42.44	38.17	30.86
	Error/(%)	-0.42	-4.51	-2.66	5.67
Total energy model	Calculated value/(MPa)	48.86	44.41	40.37	33.36
	Error/(%)	3.08	- 0.08	2.96	14.21
Static elastic modulus model	Calculated value/(MPa)	45.48	39.09	33.60	24.82
	Error/(%)	- 4.06	- 12.07	- 14.32	- 15.03
Porosity model	Calculated value/(MPa)	52.29	52.06	51.83	51.37
	Error/(%)	10.33	17.12	32.18	75.85
Wave velocity model	Calculated value/(MPa)	50.79	48.17	45.70	41.12
	Error/(%)	7.14	8.38	16.54	40.76
Dynamic-elastic modulus model	Calculated value/(MPa)	49.39	44.21	39.58	31.72
	Error/(%)	4.19	- 0.54	0.94	8.58

Table 8 Test and calculated values of peak strains after different numbers of freeze–thaw cycles

Number of freeze–thaw cycles		20	40	60	100
Test value/(%)		0.728	0.738	0.798	0.796
Dissipated energy ratio model	Calculated value/(%)	0.7296	0.748	0.808	0.786
	Error/(%)	0.22	1.36	1.25	– 1.25
Total energy model	Calculated value/(%)	0.720	0.732	0.773	0.776
	Error/(%)	– 1.99	– 0.81	– 3.13	– 2.51
Static elastic modulus model	Calculated value/(%)	0.741	0.7516	0.8442	0.809
	Error/(%)	1.79	1.84	5.79	1.63
Porosity model	Calculated value/(%)	0.7031	0.7037	0.7065	0.706
	Error/(%)	– 3.42	– 4.65	– 1.47	– 11.3
Wave velocity model	Calculated value/(%)	0.7169	0.7235	0.777	0.746
	Error/(%)	– 1.52	– 1.96	– 2.63	– 6.28
Dynamic-elastic modulus model	Calculated value/(%)	0.718	0.7251	0.781	0.783
	Error/(%)	– 1.37	– 1.75	– 2.13	– 1.63

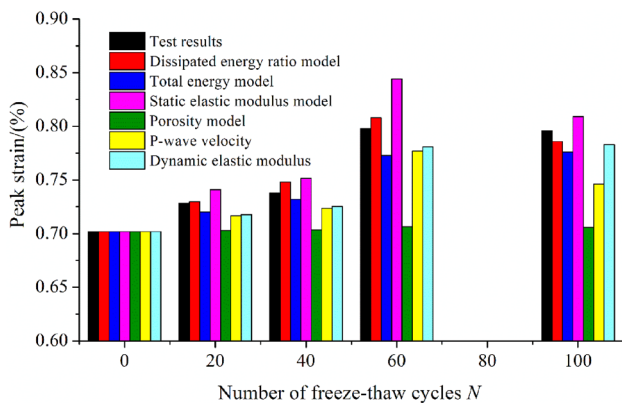


Fig. 19 Comparison diagram of the measured and calculated peak strain values

forces. Therefore, in this paper, PFC2D was used for numerical tests, with the test size of the particle flow model consistent with the indoor test size and the 2D planar model length and width being 100 and 50 mm, respectively. According to the recommendations (Potyondy and Cundall 2004) (Jin et al. 2017) for calibrating the mesoscopic parameters in the literature, (1) the particles were uniformly distributed within a radius of 0.4–0.6 mm, resulting in 5639 particles (as shown in Fig. 20), and the inter-particle parallel-bond model (Fig. 21) was used to simulate the elastic and plastic deformation processes of sandstones; (2) the effective modulus E of particles was equal to the parallel-bond effective modulus E^* , and the particle stiffness ratio k was equal to the parallel-bond stiffness ratio k^* ; and (3) the friction coefficient μ ($\mu = 0.5$) mainly affected the post-peak strength properties. The macroscopic parameters of unfrozen–thawed sandstones are shown in Table 9.

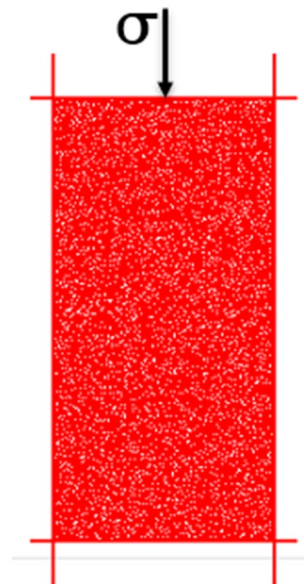


Fig. 20 Numerical model of samples

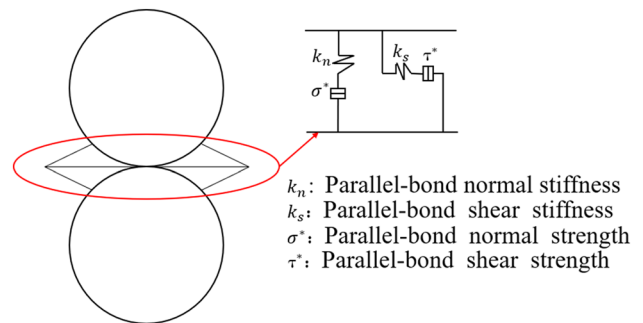
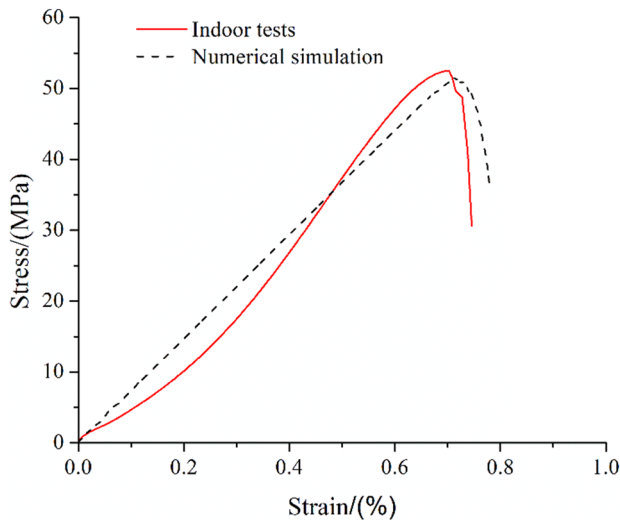


Fig. 21 Parallel-bond model

Table 9 Meso-mechanical parameters of the model

Particle density / (kg/m ³)	Particle stiffness ratio	Parallel-bond stiffness ratio	Parallel-bond normal strength/ (MPa)	Parallel-bond tangential strength/(MPa)	Effective modulus of particles/ (GPa)	Parallel-bond effective modulus/(GPa)	Friction coefficient
2500	0.65	0.65	22	27	3.2	3.2	0.5

**Fig. 22** Comparison of indoor test values and numerical simulation test values for uniaxial compression of sandstones

5.2 Results Comparison for Unfrozen–Thawed Sandstones

Based on the mesoscopic parameters in Table 9, the numerical simulation test results and indoor test results for uniaxial compression were compared, as shown in Fig. 22. The uniaxial compressive strength and peak strain obtained from the numerical simulation experiment are 51.50 MPa and 0.71%, respectively, and when compared with the indoor test results listed in Table 3, the numerical simulation test results fit better. However, according to the stress–strain curve pattern, the curve obtained from the numerical simulation is acceptable to the test curve, which is a skewed line with three points of intersection with the test curve; the curve begins to fall after exceeding the peak strength, with smaller error in this section mainly because particle shape deformation is not applied before generation of the plastic strain according to Newton's second law and force–displacement law. In general, the peak strength, peak strain, curve of the elastic stage, and curve of the plastic stage of the stress–strain curve obtained from the numerical simulation test are satisfactorily similar to the test results, demonstrating that the selected mesoscopic parameters are applicable to unfrozen–thawed sandstones.

5.3 Determination of Mesoscopic Parameters of Frozen–Thawed Sandstone

The relationship between macroscopic and mesoscopic parameters was investigated using the controlled variable method, and according to the influence of the mesoscopic parameters on the macro-parameters, the change in meso-mechanical parameters was used as an equivalent substitute for freeze–thaw actions. This simulation method has been applied in freeze–thaw cycle tests (Lin et al. 2020; Xing et al. 2020; Zhou et al. 2019). According to the literature (Guo et al. 2013; Zou and Lin, 2017), the uniaxial compressive strength of rocks is mainly influenced by parallel-bond tangential strength and parallel-bond normal strength; the Poisson's ratio of rocks is mainly influenced by the stiffness ratio. Therefore, the main mesoscopic parameters chosen for this study were the parallel-bond normal strength, parallel-bond tangential strength and stiffness ratio.

5.3.1 Parallel-Bond Normal Strength

The parallel-bond strength is divided into parallel-bond normal strength σ^* ($\sigma^* > 0$) and parallel-bond tangential strength τ^* . When the parallel-bond normal strength is greater than the tensile strength of the model, micro-cracking occurs in the model. Sensitivity analysis was performed by controlling a single variable, with other parameters in Table 9 unchanged. Only the parallel-bond normal strength was changed; i.e., the parallel-bond normal strength was set to 22, 25, 28, and 31 MPa to carry out the uniaxial compression simulation of sandstones in four different cases with different parameters to obtain different stress–strain curves, as shown in Fig. 23, and to include the parallel-bond normal strength and uniaxial compressive peak strength and peak strain of sandstones in Table 10; Figs. 24 and 25 show the fitting results of parallel-bond normal strength along with peak strength and strain, respectively.

5.3.2 Parallel-Bond Tangential Strength

The parallel-bond tangential strength τ^* acts the same as the parallel-bond normal strength σ^* , but the direction of action is different. Similarly, the initial values of other parameters in Table 9 were kept constant. The stress–strain curves of sandstones under uniaxial

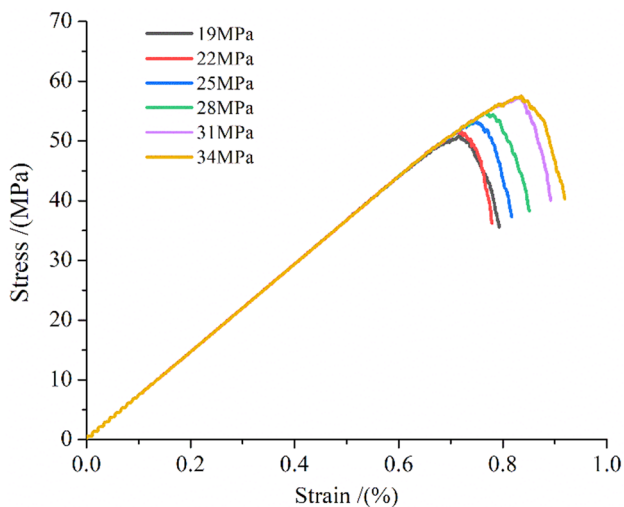


Fig. 23 Effect of parallel-bond normal strength on uniaxial compressive stress–strain curves

Table 10 Mechanical test parameters for different parallel-bond normal strengths

Parallel-bond normal strength/MPa	Peak strength/MPa	Peak strain/%
19	50.80	0.71
22	51.50	0.71
25	53.25	0.75
28	54.68	0.78
31	57.10	0.83
34	57.50	0.84

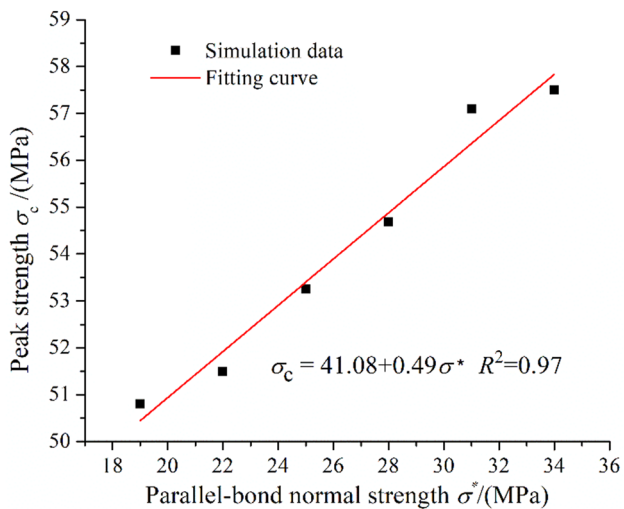


Fig. 24 Relationship between parallel-bond normal strength and peak strength

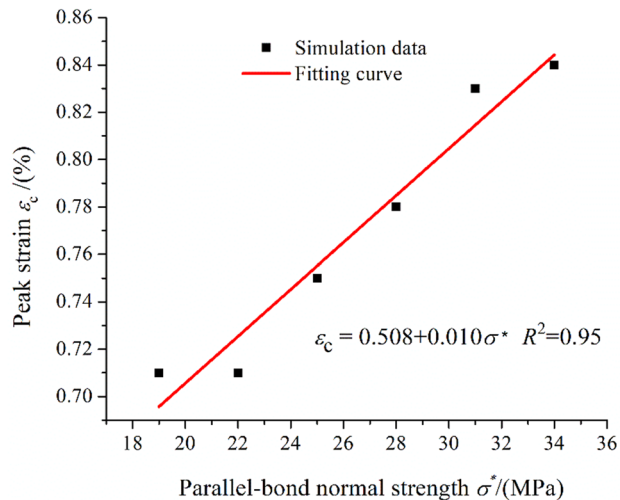


Fig. 25 Relationship between parallel-bond normal strength and peak strain

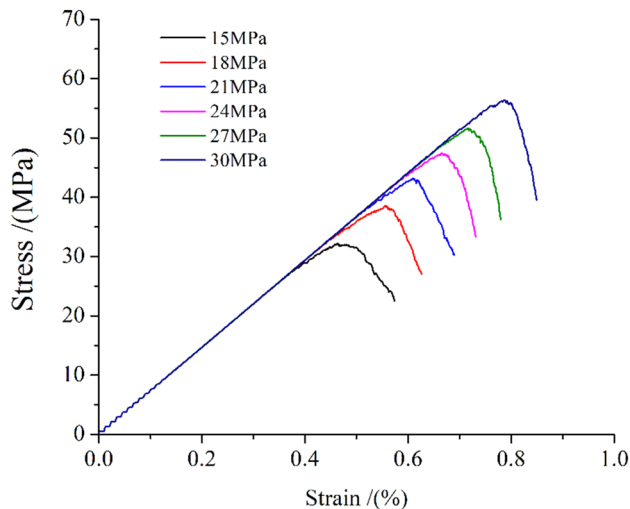


Fig. 26 Effect of parallel-bond tangential strength on uniaxial compressive stress–strain curves

compression numerical simulation are obtained when the tangential strength of the parallel bond is 18, 21, 24 and 27 MPa, as shown in Fig. 26.

The simulation results under different parallel-bond tangential strengths were further analyzed as shown in Table 11. Figures 27 and 28 show that: the uniaxial compressive strength and peak strain of sandstones showed a linear increasing relationship with the parallel-bond tangential strength. The linear equations of parallel-bond tangential strength and uniaxial compressive strength and peak strain were obtained by linear fitting to provide a foundation for calibrating the mesoscopic parameters of freeze–thaw actions.

Table 11 Mechanical test parameters for different parallel-bond tangential strengths

Parallel-bond tangential strength /MPa	Peak strength/MPa	Peak strain/%
15	32.18	46.25
18	38.50	0.558
21	43.20	0.610
24	47.47	0.664
27	51.50	0.710
30	56.41	0.788

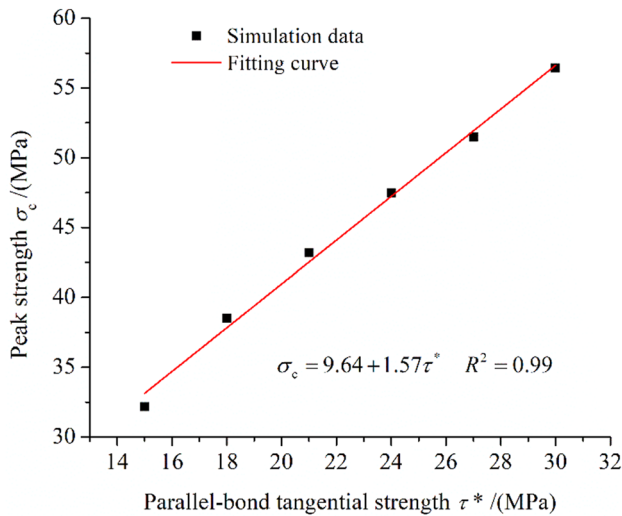


Fig. 27 Relationship between parallel-bond tangential strength and peak strength

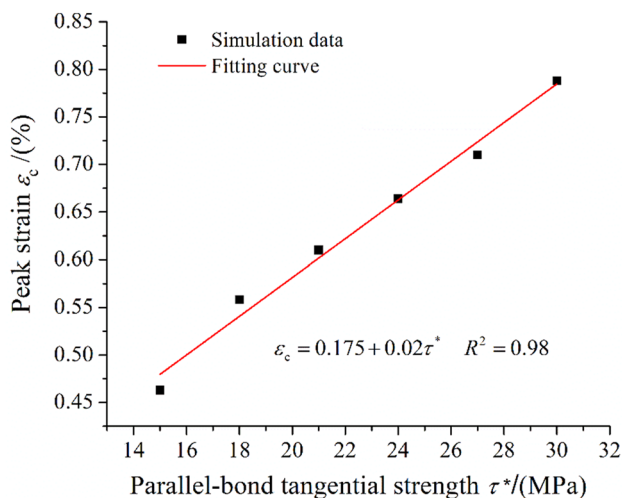


Fig. 28 Relationship between parallel-bond tangential strength and peak strain

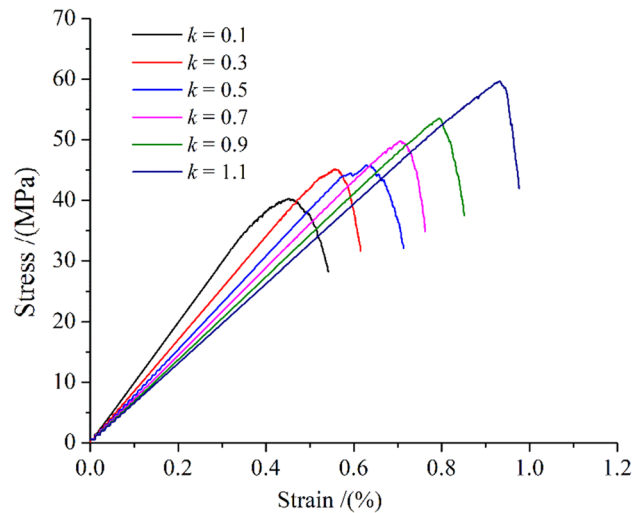


Fig. 29 Effect of stiffness ratio on uniaxial compressive stress–strain curves

Table 12 Mechanical test parameters for different parallel-bond stiffness ratios

Stiffness ratio	Peak strength/MPa	Peak strain/%
0.1	40.32	0.454
0.3	45.17	0.558
0.5	45.84	0.632
0.7	49.81	0.707
0.9	53.50	0.789
1.1	59.69	0.930

5.3.3 Stiffness Ratio

The stiffness ratio is the ratio of the normal stiffness to the tangential stiffness. The initial values of the other parameters in Table 9 were kept constant, and the stiffness ratios were set to 0.7, 1, 1.3 and 1.6. The stiffness ratios used in this model include the particle stiffness ratio k and the parallel-bond stiffness ratio k^* , which are equal in magnitude. The effect of stiffness ratios on the mechanical properties of sandstones in uniaxial compression was studied to obtain the stress–strain curves of numerical tests with different stiffness ratios (as shown in Fig. 29).

The peak strength and peak strain at different stiffness ratios are shown in Table 12. The fitting analysis results of the peak strength and peak strain versus stiffness ratio are shown in Fig. 30 and Fig. 31.

The selected mesoscopic parameters of sandstones experiencing different numbers of freeze–thaw cycles, determined by repeated numerical tests, are shown in Table 13. Figure 32 shows a comparison of the strain–stress curves of sandstones experiencing different numbers of freeze–thaw cycles derived

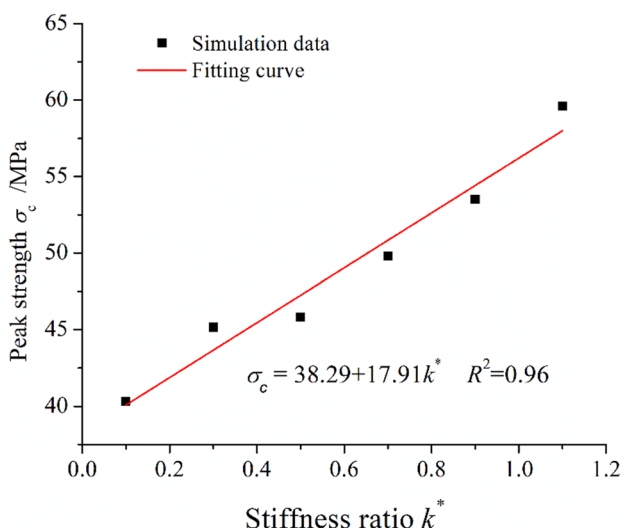


Fig. 30 Relationship between the stiffness ratio and peak strength

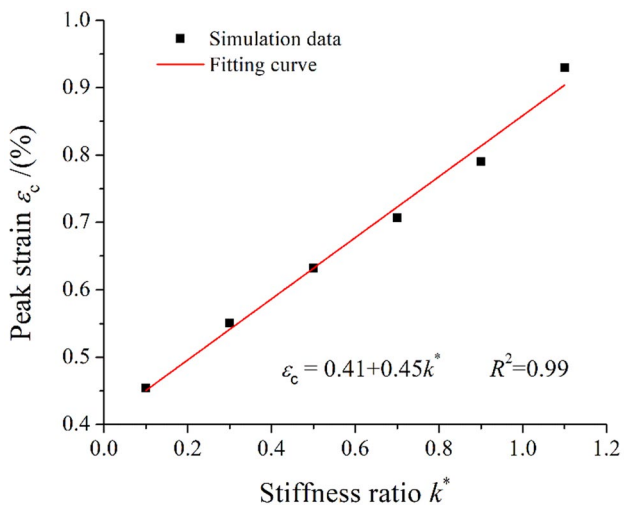


Fig. 31 Relationship between the stiffness ratio and peak strain

Table 13 Mesoscopic parameters of frozen–thawed sandstone

Number of freeze–thaw cycles	Parallel-bond normal strength / (MPa)	Parallel-bond shear strength / (MPa)	Stiffness ratio
0	22	27	0.65
20	22.5	22.5	1
40	25	19	1.3
60	32	15	1.65
100	120	5.5	2.35

from the numerical simulation model and indoor test curve. The curve derived from the numerical simulation is in good agreement with that derived from the indoor test, indicating that the parameters determined in Table 13 are valid.

The other parameters in Table 9 were kept constant to establish the relationship between the number of freeze–thaw cycles and parallel-bond normal strength, parallel-bond shear strength, and parallel-bond effective modulus, as shown in Fig. 33.

It is evident that as the number of freeze–thaw cycles increases, the parallel-bond normal strength tends to increase exponentially, the parallel-bond tangential strength tends to decrease linearly, and the stiffness ratio tends to increase linearly. Their fitting equations are as follows:

$$\sigma^* = 0.36e^{0.056N} + 21.54, \quad (R^2 = 0.99) \tag{35}$$

$$\tau^* = 27.0 - 0.21N, \quad (R^2 = 0.99) \tag{36}$$

$$k^* = 0.649 + 0.0169N, \quad (R^2 = 0.99) \tag{37}$$

According to Eqs. (35)–(37), the meso-parameter values of freeze–thaw cycling for 10, 20, 30, 50, 70, 80 and 90 cycles were calculated, as shown in Table 14, and the simulated stress–strain curve is shown in Fig. 34.

The comparative analysis of the peak stress obtained from the test and numerical simulation is shown in Fig. 35, and the comparative analysis of the peak strain is shown in Fig. 36.

It can be seen from the change in the fitting curve that the error between the test and simulation gradually increases with an increasing number of freeze–thaw cycles; however, within 100 iterations, the errors are relatively small, only 8 and 3%, respectively, indicating that the numerical simulation method is effective.

5.4 Analysis of Energy Results from Numerical Simulation

Through accuracy analysis of the above freeze–thaw damage factors, it was concluded that the dissipated energy ratio damage model has the highest accuracy. In the PFC model, the boundary energy is the action on the samples by the upper and lower loading plates. The dissipated energy consists of the energy dissipated by local damping, kinetic energy, energy dissipated by contact damping and frictional energy generated by the sliding of particles. The parallel-bond strain energy \bar{E}_k and particle bond strain energy E_k form the total strain energy:

$$U_e = \bar{E}_k + E_k \tag{38}$$

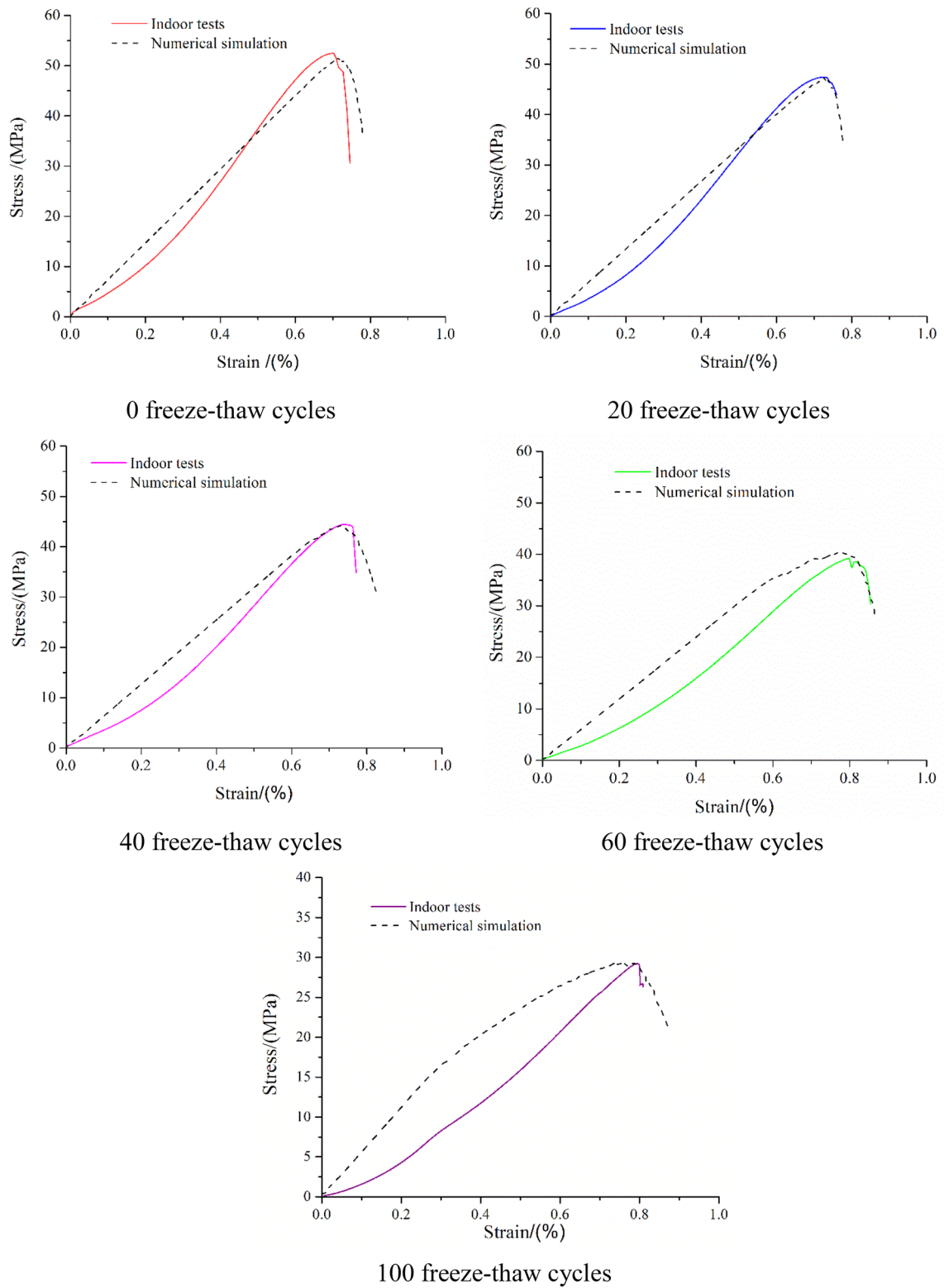


Fig. 32 Stress–strain curve of frozen–thawed sandstones after different number of freeze–thaw cycles

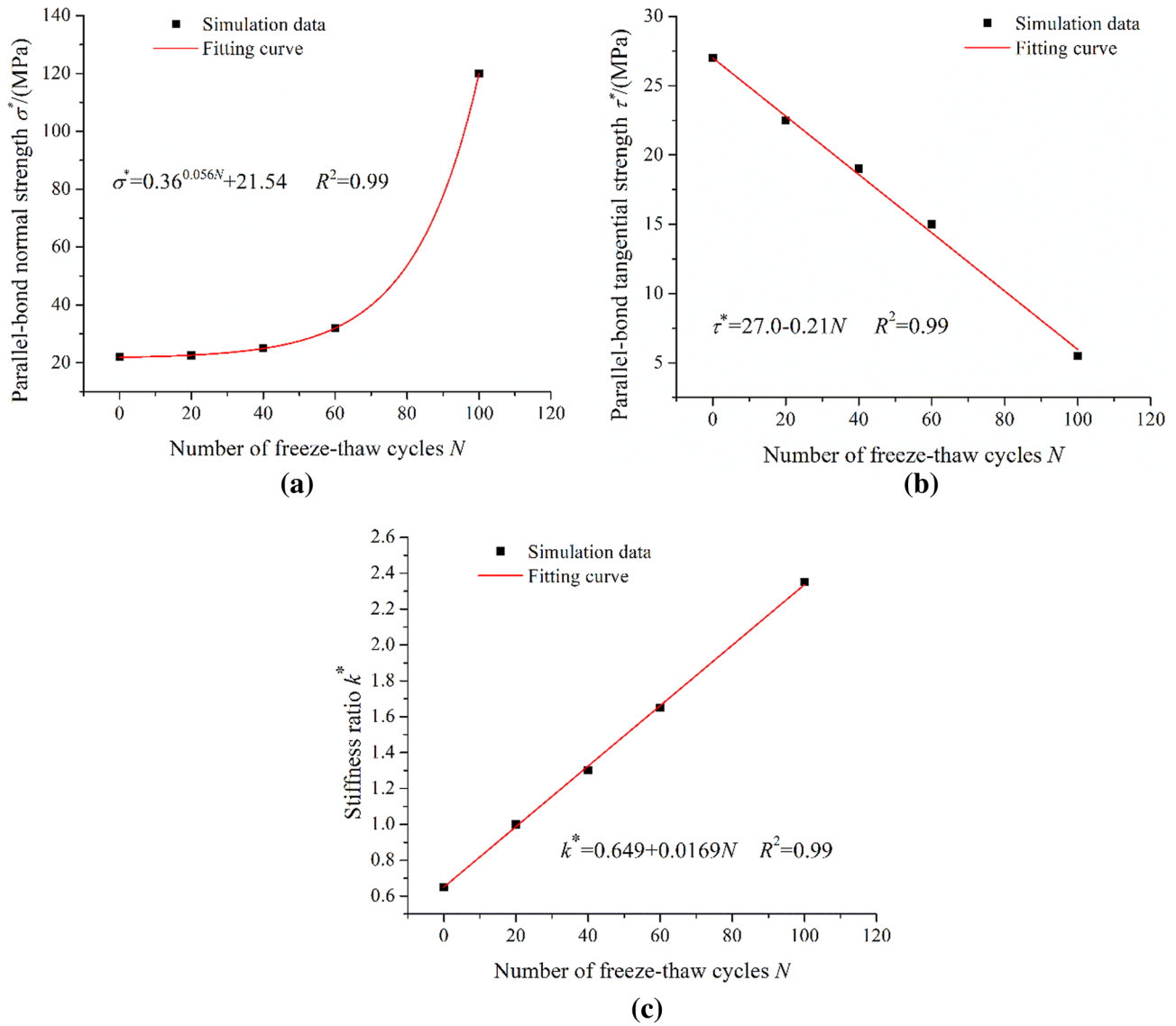


Fig. 33 **a** Relationship between the number of freeze–thaw cycles and parallel-bond normal strength; **b** relationship between the number of freeze–thaw cycles and parallel-bond tangential strength; **c** relationship between the number of freeze–thaw cycles and stiffness ratio

Table 14 Mesoscopic parameters under different freeze–thaw times

Number of freeze–thaw cycles	Parallel-bond normal strength / (MPa)	Parallel-bond shear strength / (MPa)	Stiffness ratio
10	22.17	24.9	0.82
30	23.47	20.70	1.16
50	27.46	16.5	1.49
70	39.68	11	1.83
80	52	8.5	2
90	77	6.5	2.3

$$\bar{E}_k = \frac{1}{2} \left(\frac{\bar{F}_n^2}{k_n A} + \frac{\|\bar{F}_s\|^2}{k_s A} + \frac{\bar{M}_t^2}{k_s J} + \frac{\|\bar{M}_b\|^2}{k_n I} \right) \tag{39}$$

$$E_k = \frac{1}{2} \left[\frac{(F_n)^2}{k_n} + \frac{\|F_s\|^2}{k_s} \right] \tag{40}$$

where \bar{F}_n and \bar{F}_s are the normal and tangential bond forces, respectively; k_n and k_s are the normal parallel-bond stiffness and tangential bond stiffness, respectively; A is the area of the parallel-bond cross section; \bar{M}_b and \bar{M}_t are the parallel-bond moment and torque, respectively; J is the polar

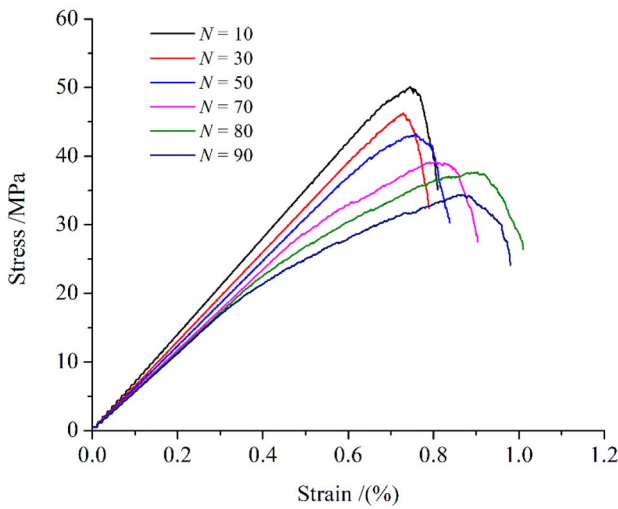


Fig. 34 Stress–strain curves under different numbers of freeze–thaw cycles

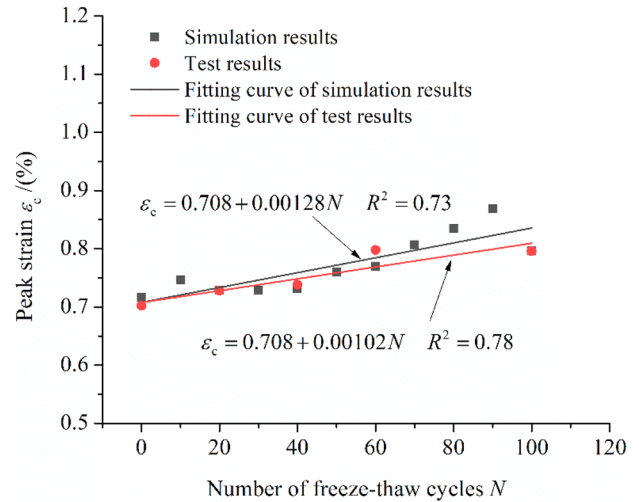


Fig. 36 Comparative analysis of peak stress

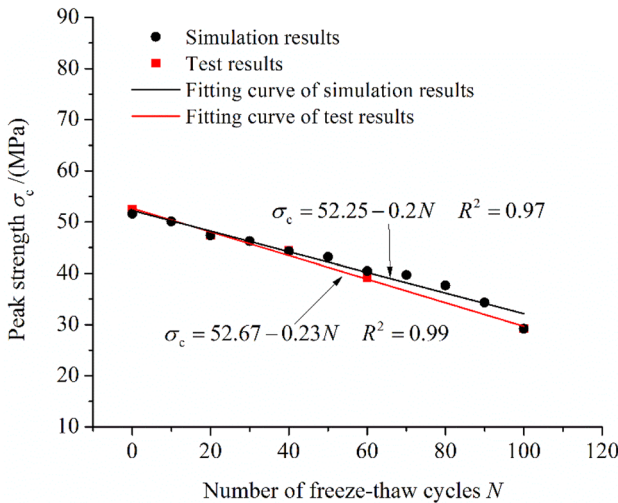


Fig. 35 Comparative analysis of peak stress

moment of inertia of the parallel-bond cross section; \bar{I} is the moment of inertia of the parallel-bond cross section; F_n and F_s are the contact forces of the normal and tangential particles, respectively; and k_n and k_s are the contact stiffness of normal and tangential particles, respectively.

Figure 37 shows the comparison of the energies derived from the test methods and numerical simulation methods. From the results, the following can be seen: The development trends of total energy, strain energy and dissipated energy are consistent, which are basically consistent with the changes in the four stages in the energy evolution law stated in Sect. 3.2.1. The pore compaction and original crack closure at the initial stage of the simulation test

failed to be simulated by the numerical simulation, leading to a slight deviation between its results and the test results. Overall, the developed numerical simulation method can simulate the mechanical laws and behaviors of the uniaxial compression of rocks during freeze–thaw cycles with a greater degree of accuracy.

6 Conclusion

Indoor tests were performed to measure the physical and mechanical properties of saturated sandstones after different numbers of freeze–thaw cycles. Freeze–thaw damage models were established based on the dissipated energy ratio, and the accuracy of these models was evaluated through comparative analysis. Eventually, a numerical simulation method for freeze–thaw damage of rocks in uniaxial compression was developed with PFC. The main research results are summarized as follows:

1. The test results of the physical and mechanical properties of saturated sandstones after freeze–thaw cycles show that the elastic modulus for every 10 freeze–thaw cycles within 100 freeze–thaw cycles decreased by 5.39%, the peak strength decreased by 4.44%, the peak strain increased by 1.34%, the P-wave velocity decreased by 2.42% and the porosity increased by 2.33%.
2. The energy evolution law of sandstones in uniaxial compression with different numbers of freeze–thaw cycles was analyzed, and a freeze–thaw damage model was established according to the relative change in the dissipated energy ratio; Peak strength and peak strain were selected as indices, and the average error of predicted value for 20, 40, 60 and 100 freeze–thaw cycles were

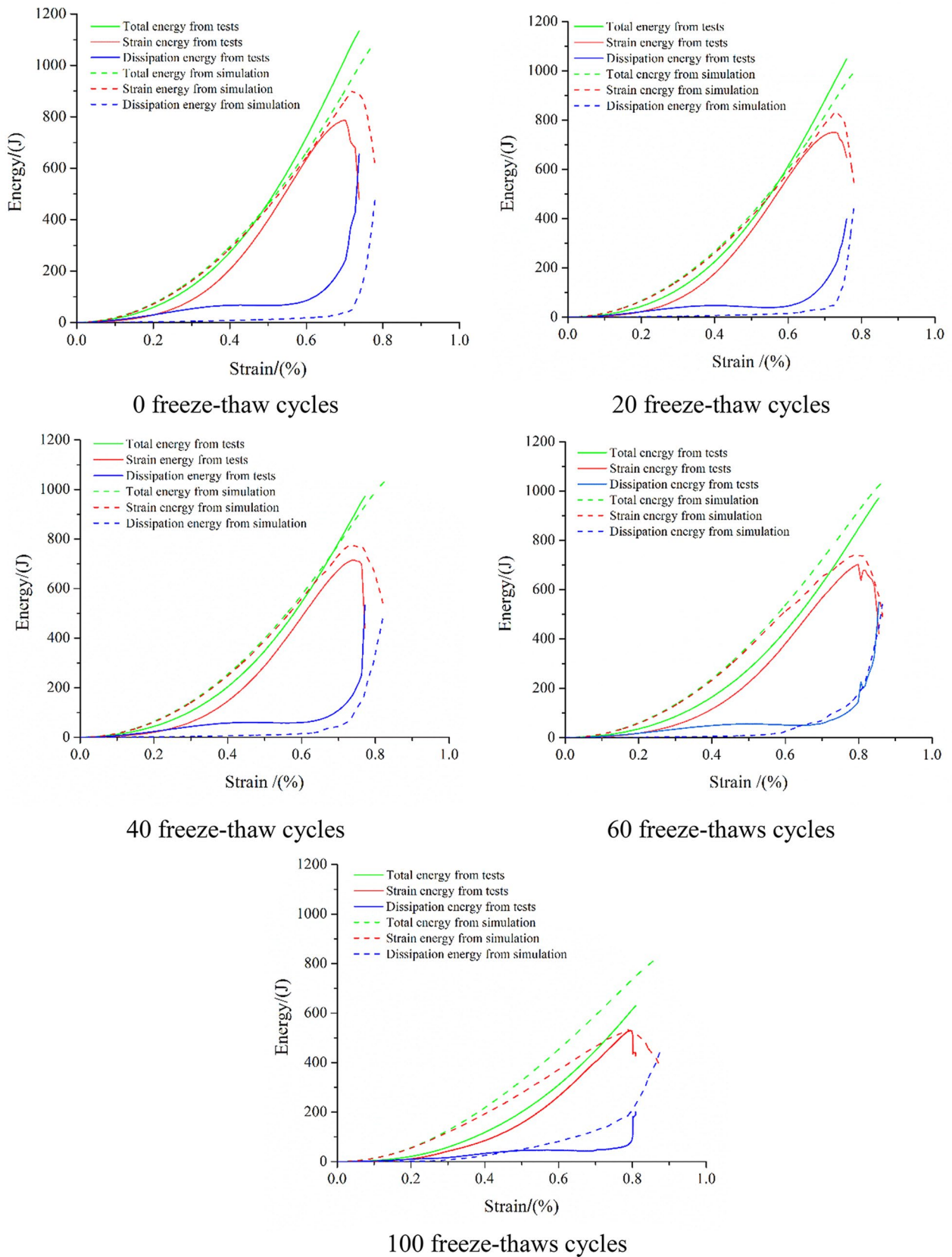


Fig. 37 Comparison of energies derived from test methods and numerical simulation methods

- 1.92 and 1.58%, respectively, which were the smallest errors among all models. The accuracy of those six models was analyzed and followed the order of dissipated energy ratio model > the dynamic elastic modulus model > the total energy model > the static elastic modulus model > the P-wave velocity model > the porosity model.
3. According to the experimental and computational results from the numerical simulation, the parallel-bond normal strength and the number of freeze–thaw cycles have an exponential relationship, the parallel-bond tangential strength and the number of freeze–thaw cycles have a linear decreasing relationship, and the stiffness ratio and the number of freeze–thaw cycles have a linear increasing relationship. The deterioration effect of freeze–thaw cycles on saturated sandstone is reflected by the change in these three parameters. The simulated stress–strain curve was compared with the test curve to verify that the established numerical simulation method of uniaxial compression for rock damaged by freezing–thawing is highly reliable.
 4. The numerical method was used to calculate the total energy, elastic strain energy and dissipated energy of sandstones in uniaxial compression under different numbers of freeze–thaw cycles and was verified with the test results. Such a simulation method can simulate the mechanical laws and behaviors of uniaxial compression of rocks during freeze–thaw cycles with a greater degree of accuracy. Therefore, this study may prove useful for analyzing of the mechanism of the freeze–thaw damage of rocks and could guide engineering designs for cold weather regions.

Acknowledgements This work was supported by the Natural Science Foundation of Shandong Province (ZR2016JL018), Research and Innovation Team Project of College of Civil Engineering and Architecture, Shandong University of Science and Technology (2019TJKYTD02), and Project of Shandong Province Higher Educational Young Innovative Talent Introduction and Cultivation Team (Disaster prevention and control team of underground engineering involved in sea).

Author Contributions QF: Supervision, Conceptualization, Writing—review and editing. JJ: Formal analysis, Methodology, Software, Writing—original draft. SZ: Validation, Software. WL: Conceptualization, Data curation, Writing—review. XY: Resources, Validation. WL: Investigation.

Declarations

Conflict of Interest The authors declare that they have no known competing financial interests or personal relationships that could have appeared to influence the work reported in this paper.

References

- Altindag R, Alyildiz IS, Onargan T (2004) Mechanical property degradation of ignimbrite subjected to recurrent freeze–thaw cycles. *Int J Rock Mech Min Sci* 41(6):1023–1028. <https://doi.org/10.1016/j.ijrmms.2004.03.005>
- Bai SH (2015) Experimental study on energy evolution and damage characteristics of fractured rock mass under cyclic loading. Chengdu University of Technology (in Chinese)
- Chen W, Konietzky H, Tan X, Frühwirth T (2016) Pre-failure damage analysis for brittle rocks under triaxial compression. *J Comput Geotech* 74:45–55. <https://doi.org/10.1016/j.compgeo.11.018>
- Deng HW, Yu S, Deng J, Ke B, Bin F (2019) Experimental investigation on energy mechanism of freezing–thawing treated sandstone under uniaxial static compression. *KSCE J Civ Eng* 23(5):2074–2082. <https://doi.org/10.1007/s12205-019-1278-5>
- Duan A, Chen J, Jin WL (2013) Numerical simulation of the freezing process of concrete. *J Mater Civ Eng* 25(9):1317–1325. [https://doi.org/10.1061/\(ASCE\)MT.1943-5533.0000655](https://doi.org/10.1061/(ASCE)MT.1943-5533.0000655)
- Fan L, Li FH, Zhang YW, Cui SA, Li JL (2013) Research into the concrete freeze–thaw damage mechanism based on the principle of thermodynamics. *J Constr Build Mater* 357–360:751–756. <https://doi.org/10.1016/10.4028/www.scientific.net/AMM.357-360.751>
- Gao F, Cao S, Zhou K, Lin Y, Zhu L (2020) Damage characteristics and energy-dissipation mechanism of frozen–thawed sandstone subjected to loading. *J Cold Reg Sci Tech* 169(2020):102920. <https://doi.org/10.1016/j.coldregions.2019.102920>
- Guo J, Xu G, Jing H, Kuang T (2013) Fast determination of meso-level mechanical parameters of PFC models. *Int J Min Sci Tech* 23(1):157–162. <https://doi.org/10.1016/j.ijmst.03.007>
- Hassanzadegan A, Blöcher G, Milsch H (2014) The effects of temperature and pressure on the porosity evolution of flechtinger sandstone. *J Rock Mech Rock Eng* 47(2):421–434
- Huang YH, Yang SQ, Ranjith PG, Zhao J (2017) Strength failure behavior and crack evolution mechanism of granite containing pre-existing non-coplanar holes. *J Comput Geotech* 88:182–198. <https://doi.org/10.1016/j.compgeo.2017.03.015>
- Inserra C, Biwa S, Chen Y (2013) Influence of thermal damage on linear and nonlinear acoustic properties of granite. *J Int J Rock Mech Min Sci* 62:96–104. <https://doi.org/10.1016/j.ijrmms.2013.05.001>
- Jia HL, Xiang W, Krautblatter M (2015) Quantifying rock fatigue and decreasing compressive and tensile strength after repeated freeze–thaw cycles. *J Permafrost Periglacial Process* 26:368–377. <https://doi.org/10.1002/ppp.1857>
- Jin J, Cao P, Chen Y, Pu C, Mao D, Fan X (2017) Influence of single flaw on the failure process and energy mechanics of rock-like material. *J Comput Geotech* 86:150–162. <https://doi.org/10.1016/j.compgeo.01.011>
- Kachanov LM (1958) Time of the rupture process under creep conditions. *J Izv Akad Nauk SSR Otd Tech Nauk* 8:26–31
- Kawamoto T, Ichikawa Y, Kyoya T (1988) Deformation and fracturing behaviour of discontinuous rock mass and damage mechanics theory. *Int J Numer Anal Methods Geomech*. 12(1):1–30. <https://doi.org/10.1002/nag.1610120102>
- Ke B, Zhou K, Deng H, Bin F (2017) NMR pore structure and dynamic characteristics of sandstone caused by ambient freeze–thaw action. *J Shock Vib* 2017(4):1–10. <https://doi.org/10.1155/2017/9728630>
- Khazaei C, Hazzard J, Chalaturnyk R (2015) Damage quantification of intact rocks using acoustic emission energies recorded during uniaxial compression test and discrete element modeling. *J Comput Geotech* 67:94–102. <https://doi.org/10.1016/j.compgeo.2015.02.012>
- Krautblatter M, Funk D, Günzel FK (2013) Why permafrost rocks become unstable: a rock-ice-mechanical model in time and space.

- J Earth Surf Process Landf 38(8):876–887. <https://doi.org/10.1002/esp.3374>
- Lemaitre J (1984) How to use damage mechanics. *J Nucl Eng Des* 80(2):233–245. [https://doi.org/10.1016/0029-5493\(84\)90169-9](https://doi.org/10.1016/0029-5493(84)90169-9)
- Li JL, Kaunda RB, Zhou KP (2018) Experimental investigations on the effects of ambient freeze–thaw cycling on dynamic properties and rock pore structure deterioration of sandstone. *J Cold Reg Sci Technol* 154:133–141. <https://doi.org/10.1016/j.coldregions.2018.06.015>
- Lin H, Lei D, Yong R, Jiang C, Du S (2020) Analytical and numerical analysis for frost heaving stress distribution within rock joints under freezing and thawing cycles. *J Environ Earth Sci*. <https://doi.org/10.1007/s12665-020-09051-x>
- Liu Q, Huang S, Kang Y, Liu X (2015) A prediction model for uniaxial compressive strength of deteriorated rocks due to freeze–thaw. *J Cold Reg Sci Tech* 120:96–107. <https://doi.org/10.1016/j.coldregions.2015.09.013>
- Liu WW, Feng Q, Wang CX, Lu CK, Xu ZZ, Li WT (2019) Analytical solution for three-dimensional radial heat transfer in a cold region tunnel. *J Cold Reg Sci Technol* 164:1–12. <https://doi.org/10.1016/j.coldregions.2019.102787>
- Matsuoka N (1990) Mechanisms of rock breakdown by frost action: an experimental approach. *Cold Reg Sci Technol* 17:253–270. [https://doi.org/10.1016/s0165-232x\(05\)80005-9](https://doi.org/10.1016/s0165-232x(05)80005-9)
- Mutlutürk M, Altindag R, Türk G (2004) A decay function model for the integrity loss of rock when subjected to recurrent cycles of freezing–thawing and heating–cooling. *Int J Rock Mech Min Sci* 41(2):237–244. [https://doi.org/10.1016/S1365-1609\(03\)00095-9](https://doi.org/10.1016/S1365-1609(03)00095-9)
- Pan WH, Sun XD, Wu LM, Yang KK, Tang N (2019) Damage detection of asphalt concrete using piezo-ultrasonic wave technology. *J Mater*. <https://doi.org/10.3390/ma12030443>
- Petersen L, Lohaus L, Polak MA (2007) Influence of freezing -and -thawing damage on behavior of reinforced concrete elements. *J ACI Mater J* 104(4):369–378
- Potyondy DO, Cundall PA (2004) A bonded-particle model for rock. *Int J Rock Mech Min Sci* 41(8):1329–1364. <https://doi.org/10.1016/j.ijrmm.2004.09.011>
- Pudasaini SP, Krautblatter M (2014) A two-phase mechanical model for rock-ice avalanches. *J Geophys Res Earth* 119(10):2272–2290. <https://doi.org/10.1002/2014jf003183>
- Qiu WL, Teng F, Teng SS (2020) Damage constitutive model of concrete under repeated load after seawater freeze–thaw cycles. *J Constr Build Mater* 236:117560. <https://doi.org/10.1016/j.conbuilmat.2019.117560>
- Remy JM, Bellanger M, Homand-Etienne F (1994) Laboratory velocities and attenuation of P-waves in limestones during freeze–thaw cycles. *J Geophys* 59:245–251. <https://doi.org/10.1190/1.1443586>
- Takarli M, Pince W, Siddique R (2008) Damage in granite under heating/cooling cycles and water freeze–thaw condition. *J Int J Rock Mech Min Sci* 45:1164–1175. <https://doi.org/10.1016/j.ijrmm.2008.01.002>
- Tan X, Chen W, Yang J, Cao JJ (2011) Laboratory investigations on themechanical properties degradation of granite under freeze-thaw cycles. *J Cold Reg Sci Tech* 68(3):130–138. <https://doi.org/10.1016/j.coldregions.2011.05.007>
- Wang S, Qi J, Yu F, Liu F (2016) A novel modeling of settlement of foundations in permafrost regions. *J Geomech Eng* 10(2):225–245. <https://doi.org/10.12989/gae.2016.10.2.225>
- Wang P, Xu JY, Fang XY, Wang PX (2017) Energy dissipation and damage evolution analyses for the dynamic compression failure process of red-sandstone after freeze-thaw cycles. *J Eng Geol* 221:104–113. <https://doi.org/10.1016/j.enggeo.2017.02.025>
- Wang C, Zhan SF, Xie MZ, Wang C, Cheng LP, Xiong ZQ (2020) Damage characteristics and constitutive model of deep rock under frequent impact disturbances in the process of unloading high static stress. *J Complexity* 2020:1–15. <https://doi.org/10.1155/2020/2706091>
- Xie HP, Ju Y, Li LY (2005) Criteria for strength and structural failure of rocks based on energy dissipation and energy release principles. *J Cold Reg Sci Tech* 24(17):3003–3010. <https://doi.org/10.3321/j.issn:1000-6915.2005.17.001>
- Xing K, Zhou Z, Yang H, Liu B (2020) Macro–meso freeze–thaw damage mechanism of soil–rock mixtures with different rock contents. *Int J Pavement Eng* 21(1):9–19. <https://doi.org/10.1080/10298436.2018.1435879>
- Yang SQ, HuangM YH, Jing HW, Liu XR (2014) Discrete element modeling on fracture coalescence behavior of red sandstone containing two unparallel fissures. *J Eng Geol* 178:28–48. <https://doi.org/10.1016/j.enggeo.2014.06.005>
- Zhang HM, Wang H, Zhang JF, Cheng SF, Zhou HW (2020) Analysis of meso-damage characteristics of freeze-thaw rocks at CT scale. *J Liaoning Tech Univ (nat Sci Ed)* 39(01):51–56. <https://doi.org/10.11956/j.issn.1008-0562.2020.01.008> (in Chinese)
- Zhou Z, Xing K, Yang H, Wang H (2019) Damage mechanism of soil-rock mixture after freeze–thaw cycles. *J Central South Univ* 26(1):13–24. <https://doi.org/10.1007/s11771-019-3979-9>
- Zou Q, Lin B (2017) Modeling the relationship between macro- and meso-parameters of coal using a combined optimization method. *J Environ Earth Sci* 76(14):479.1–479.20. <https://doi.org/10.1007/s12665-017-6816-1>
- Zuber B, Marchand J (2004) Predicting the volume instability of hydrated cement systems upon freezing using poro-mechanics and local phase equilibria. *J Mater Struct* 37(268):257–270. <https://doi.org/10.1007/BF02480634>

Publisher's Note Springer Nature remains neutral with regard to jurisdictional claims in published maps and institutional affiliations.